Assessing the Performance of the ADAPT and AFT Flux Transport Models Using In-Situ Measurements From Multiple Satellites

KALMAN J. KNIZHNIK, MICAH J. WEBERG, ELENA PROVORNIKOVA, HARRY P. WARREN, MARK G. LINTON, SHAHEDA BEGUM SHAIK, YUAN-KUEN KO, SAMUEL J. SCHONFELD, IGNACIO UGARTE-URRA, AND LISA A. UPTON SAMUEL J. SCHONFELD, WARREN, MICHAEL SAMUEL J. SCHONFELD, IGNACIO UGARTE-URRA, AND LISA A. UPTON SAMUEL J. SCHONFELD, WARREN, MICHAEL SAMUEL J. SCHONFELD, WARREN, WARR

Naval Research Laboratory, 4555 Overlook Avenue SW, Washington, DC 20375, USA
 ² George Mason University, 4400 University Dr, Fairfax, VA 22030
 ³ Johns Hopkins Applied Physics Laboratory, 11100 Johns Hopkins Road, Laurel, MD 20723, USA
 ⁴ Air Force Research Laboratory, Space Vehicles Directorate, Kirtland AFB, NM 87117, USA
 ⁵ Space Systems Research Corporation, 1940 Duke Street Suite 200, Alexandria, Virginia 22314, USA

ABSTRACT

The launches of Parker Solar Probe (Parker) and Solar Orbiter (SolO) are enabling a new era of solar wind studies that track the solar wind from its origin at the photosphere, through the corona, to multiple vantage points in the inner heliosphere. A key ingredient for these models is the input photospheric magnetic field map that provides the boundary condition for the coronal portion of many heliospheric models. In this paper, we perform steady-state, data-driven magnetohydrodynamic (MHD) simulations of the solar wind during Carrington rotation 2258 with the GAMERA model. We use the ADAPT and AFT flux transport models and quantitatively assess how well each model matches in-situ measurements from Parker, SolO, and Earth. We find that both models reproduce the magnetic field components at Parker quantitatively well. At SolO and Earth, the magnetic field is reproduced relatively well, though not as well as at Parker, and the density is reproduced extremely poorly. The velocity is overpredicted at Parker, but not at SolO or Earth, hinting that the Wang-Sheeley-Arge (WSA) relation, fine-tuned for Earth, misses the deceleration of the solar wind near the Sun. We conclude that AFT performs quantitatively similarly to ADAPT in all cases and that both models are comparable to a purely WSA heliospheric treatment with no MHD component. Finally, we trace field lines from SolO back to an active region outflow that was observed by Hinode/EIS, and which shows evidence of elevated charge state ratios.

Keywords: Sun: corona – Sun: heliosphere – Sun: solar wind

1. INTRODUCTION

Understanding how the solar wind is heated and accelerated is one of the most important open questions in heliophysics. It is well established that the high-speed solar wind that permeates much of the heliosphere originates in large coronal holes (Hundhausen 1977; Zirker 1977), while there is also a slow-speed solar wind that appears to be partly formed by the interaction of closed field regions on the Sun with neighboring open field lines

¹, often called interchange reconnection (Gosling 1997; Antiochos et al. 2011). Thus the properties of the solar wind are tied to its magnetic origin and tracking solar wind streams back to the solar surface is critical for advancing our understanding of plasma processes on open field lines.

Since the 1970s, space missions have been providing solar wind plasma and magnetic field measurements from near Earth at 1 astronomical unit (AU; 1 AU =

Corresponding author: K. J. Knizhnik kalman.knizhnik@nrl.navy.mil

¹ Technically, "closed" field lines are those that leave and return to the photospheric surface within an Alfvén surface (spanned by all points where $V_r = V_A$, with V_A the Alfvén speed) since field lines extending beyond this radius ("open" field lines) cannot communicate information via Alfvén waves back to the surface. However, in potential field source surface models (Section 2.3 and Section 4), all field lines extending beyond the source surface are considered "open".

 $215R_{\odot}$, where $R_{\odot}=697$ Mm) from the Sun. Satellites such as the International Monitoring Platform-8 (IMP-8; Paularena & King 1999), International Sun-Earth Explorer-3 (ISEE-3; Ogilvie et al. 1978), Wind (Szabo 2015), Solar and Heliospheric Observatory (SOHO; Domingo et al. 1995), and Advanced Composition Explorer (ACE; Stone et al. 1998) have measured plasma properties near Earth. The Solar Terrestrial Relations Observatory (STEREO; Driesman et al. 2008) measured plasma properties off the Sun-Earth line at 1 AU. Helios (Jackson 1985) measured plasma properties down to 0.3 AU. Ulysses (Wenzel et al. 1992) measured plasma properties out of the ecliptic.

The recent launch of Parker Solar Probe (Parker; Fox et al. 2016) and Solar Orbiter (SolO; Müller et al. 2013, 2020) have heralded a new era for solar and heliospheric science thanks to their unique orbits and synergetic measurements from various positions in the inner heliosphere. Parker was launched on 2018 August 12 and is designed to go within 9 solar radii (R_{\odot}) of the solar surface, marking the closest approach ever of an artificial satellite to the Sun. It carries a state-of-the-art suite of instruments for both remote sensing (WISPR; Vourlidas et al. 2016) and in-situ (FIELDS; Bale et al. 2016), (SWEAP; Kasper et al. 2016), (IS⊙IS; McComas et al. 2016) measurements. Parker measurements have been used to constrain photospheric flux transport models (e.g., Wallace et al. 2022) and coronal heating rates in the solar wind using simultaneous remote sensing and in-situ measurements from SolO (e.g., Telloni et al. 2023). For a recent review of Parker Solar Probe's discoveries, see Raouafi et al. (2023).

SolO was launched on 2020 February 10 and will reach a perihelion of about 60 solar radii. While Parker will remain very close to the ecliptic plane, the inclination of SolO's orbit will increase by repeated gravitational interactions with Venus. During its extended mission phase, SolO will reach latitudes of more than 30° above the ecliptic. SolO carries suites of instruments for both remote sensing and in-situ observations such as SWA (Owen et al. 2020) and MAG (Müller et al. 2013; Horbury et al. 2020).

This new era for solar and heliospheric science is further afforded by a slew of cotemporaneous solar observations from both space-based and ground-based observatories. Of particular importance are spectroscopic observations from instruments such as the EUV Imaging Spectrometer (EIS; Culhane et al. 2007) onboard Hinode (Kosugi et al. 2007) and the Interface Region Imaging Spectrograph (IRIS; De Pontieu et al. 2014) and the Spectral Imaging of the Coronal Environment (SPICE; SPICE Consortium et al. 2020) onboard SolO, which are

capable of detecting dynamic properties of the plasma in the solar upper atmosphere such as thermal/non-thermal motions and outflows. Imaging observations from instruments such as the Atmospheric Imaging Assembly (AIA; Lemen et al. 2012) onboard the Solar Dynamics Observatory (SDO), Extreme Ultraviolet Imager (EUVI; Howard et al. 2008) on STEREO and the Solar Orbiter Extreme Ultraviolet Imager (EUI; Rochus et al. 2020) provide an important context of the dynamics in the solar atmosphere.

Due to the observational gap in space between the remote-sensed solar observations and the in-situ measurements in the inner heliosphere, modeling is still required to link the solar wind measured in situ back to its origin at the Sun. Most such models consist of two parts: 1) a coronal model, with the photospheric magnetic field as its inner boundary condition, spanning from the photosphere up to 0.1 AU, coupled with 2) an inner heliospheric model (loosely defined here as between 0.1-1 AU), where the outer boundary of the coronal model at 0.1 AU is the inner heliospheric model's inner boundary.

Coronal models actually start at the photosphere, where remote sensing instruments such as the Helioseismic and Magnetic Imager (HMI) (Scherrer et al. 2012) provide photospheric magnetograms, maps of the photospheric radial magnetic field, that are used as a boundary condition for the coronal model. Multiple magnetograms taken over an extended time period can be combined into a single "synoptic" map. Synoptic maps are traditionally constructed by taking a strip at the central meridian from Earth over the course of a full solar rotation and stacking these up horizontally to create an approximate map of the full sun over that time period (Harvey et al. 1980; Ulrich & Boyden 2006). Since the photospheric magnetic field is continuously evolving, techniques to dynamically evolve flux have been developed in order to transport flux self-consistently around the solar surface. This permits the creation of a "synchronic map", which shows the full Sun at a single instant in time, where the Earth side view of the Sun is a Carrington projected assimilation of a full disk magnetogram of that instant, and the remaining unobserved area is populated with transported magnetic flux from a synchronic map of a previous instant. These flux transport models typically differ in how new data is assimilated into the map, and what physical processes are modeled (Arge et al. 2010; Upton & Hathaway 2014). To a large extent, as will be described below, the output of coronal and heliospheric modeling is only as good as these input flux transport maps. It is therefore crucial to determine the most accurate boundary condition for the coronal models. Each coronal model, in turn, can

have various degrees of complexity in their treatment of coronal physics, ranging from potential field source surface (PFSS; Altschuler & Newkirk 1969; Schatten et al. 1969) models to magnetohydrodynamic (MHD) models. PFSS models are typically combined with a Schatten current sheet (SCS) model to connect the source surface (usually defined as a sphere concentric on the Sun at a distance around $2.5R_{\odot}$ from Sun center; Altschuler & Newkirk 1969) to the inner heliosphere and beyond. The Wang-Sheeley-Arge model (WSA; Wang & Sheeley 1990; Arge & Pizzo 2000) is used to relate the magnetic field structure inside the source surface to the plasma properties at and beyond 0.1 AU. Using WSA², therefore, enables models to bypass running a full MHD simulation out to 0.1 AU. Meanwhile, coronal MHD models such as MAS/CORHEL (Riley et al. 2012; Lionello et al. 2014), AWSoM (van der Holst et al. 2014), COCONUT (Perri et al. 2022) and MULTI-VP (Pinto & Rouillard 2017) solve the MHD equations inside 0.1 AU and can be fed directly into inner heliospheric models.

Inner heliospheric models can also have various degrees of complexity in their treatment of inner heliospheric physics, ranging from ballistic propagation to MHD simulations. In ballistic models (Nolte & Roelof 1973; Badman et al. 2020, 2021, 2022, 2023), the magnetic field outside the coronal model is taken to follow a Parker spiral so that magnetic field lines can be traced from anywhere in the heliosphere ballistically back to 0.1 AU, and then to the photosphere. Meanwhile, MHD models such as the inner heliospheric versions of MAS and AWSoM, as well as EUHFORIA (Pomoell & Poedts 2018), or ENLIL (Odstroil 2003) predict the inner heliospheric environment of the solar wind and the propagation of CMEs within it by taking the output from coronal models as input and are also well-suited for tracing the solar wind/open field from any location back to its footpoint at the solar surface.

Previous work has tested various models against each other using various statistical techniques (MacNeice et al. 2011; Riley et al. 2013; Samara et al. 2021; Jivani et al. 2023), and has produced impressive comparisons between in-situ Parker data and single-fluid MHD models (Kim et al. 2020; Pogorelov 2020; Riley et al. 2021; van der Holst et al. 2022), two fluid MHD models (Chhiber et al. 2021), as well as ballistic models (Nolte & Roelof 1973; Badman et al. 2020, 2021, 2022, 2023). MHD models have also been used successfully to predict

CME signatures at 1 AU (Wu & Dryer 1997; Wu et al. 2007, 2011, 2016a,b, 2020).

One important challenge in any model that relates remote sensing observations with in-situ predictions or measurements of solar wind properties is accurately connecting the in-situ data with its source location on the Sun. The most direct way to do this is by tracing magnetic field lines in order to map plasma from the inner heliosphere to the photosphere. In practice, this mapping depends on the combination of models used to extrapolate the photospheric magnetic field into the inner heliosphere. A recent study (Badman et al. 2023) compared four different approaches to obtaining the source locations of plasma measured by Parker during its 10th perihelion pass. The four approaches were 1) a pure WSA model out to $21.5R_{\odot}$ with a ballistic heliospheric model beyond that, 2) a PFSS model to the source surface and a ballistic heliospheric model beyond that, 3) a MHD/ballistic model inside/outside $30R_{\odot}$ and 4) a WSA model to $10R_{\odot}$ and an MHD model outside $10R_{\odot}$. The authors find that the models result in approximately the same source regions when solar activity is low and there are plenty of equatorial coronal holes to warp the heliospheric current sheet away from Parker so that small differences between the models do not encounter any magnetic separatrices.

In this paper, we present a new coupled coronal and inner heliospheric model suite, namely WSA+Grid Agnostic MHD for Extended Research Applications (GAM-ERA; Zhang et al. 2019; Sorathia et al. 2020; Mostafavi et al. 2022), and model the evolution of the heliosphere during Carrington Rotation (CR) 2258. One major difference between our model and previous iterations of the WSA+MHD combination of models (e.g., Odstrcil 2003, with ENLIL), Wu et al. (2016a,b, 2020) with the H3DMHD code and Kim et al. (2020) with the MS-FLUKSS code as the MHD component of the coupled model is our use of the Advective Flux Transport (AFT) model (Upton & Hathaway 2014; Ugarte-Urra et al. 2015; Upton & Hathaway 2018), in addition to the commonly used Air Force Data Assimilative Photospheric Flux Transport (ADAPT) model (Arge et al. 2010, 2013; Hickmann et al. 2015) to seed the magnetic field and velocity state of the low corona and inner heliosphere. In this paper, we use both ADAPT and AFT to obtain predictions at various satellites in the inner heliosphere. We quantitatively compare MHD and WSA heliospheric models whose coronal portion is determined from the ADAPT and AFT models by studying the insitu measurements at Parker, SolO, and Earth. Finally, we make use of the composition instrumentation on SolO (SWA-HIS; Livi et al. 2023) to map and validate SolO's

 $^{^2}$ In this paper, the WSA model will henceforth be assumed to include the SCS in the coronal portion of the model. Thus, writing 'WSA' implicitly assumes the presence of the SCS from R_{ss} outward.

magnetic connectivity to a source region on the Sun that was observed in a Hinode/EIS raster. Validation of these connectivity models is critical for understanding solar wind acceleration and heating.

This paper is organized as follows. In Section 2 we describe our models connecting the photosphere to the source surface, 0.1 AU, and then 1 AU. In Section 3, we compare the model results with the in-situ measurements by Parker, SolO, and spacecraft at Earth and trace the open magnetic field lines from these spacecraft locations to the source regions of the solar wind. In Section 4, we discuss some of the implications and interpretations of our results.

2. NUMERICAL MODEL

2.1. The GAMERA Model

GAMERA is an MHD solver with numerical algorithms inherited from the Lyon-Fedder-Mobary (LFM; Lyon et al. 2004) MHD code which features high-order spatial reconstruction in arbitrary non-orthogonal curvilinear coordinates and a constrained transport method fulfilling the $\nabla \cdot \mathbf{B} = 0$ condition to machine precision. Following the application of the LFM code to simulations of the inner heliosphere (Merkin et al. 2016; Merkin et al. 2016; Merkin et al. 2011), it was rewritten as GAMERA for magnetospheric applications. GAMERA, in turn, has recently been used to model the solar wind in the steady state inner heliosphere to study the generation of the Kelvin-Helmholtz instability (Mostafavi et al. 2022). Compared to LFM, GAMERA includes upgrades in the numerical scheme, improvements in code implementation, and hybrid parallelism using MPI and OMP. GAMERA was designed to be portable and optimized for modern supercomputer architectures while maintaining the algorithmic features of LFM.

GAMERA solves the semi-conservative ideal MHD equations having the form:

$$\frac{\partial \rho}{\partial t} = -\nabla \cdot (\rho \mathbf{v}),\tag{2.1}$$

$$\frac{\partial \rho \mathbf{v}}{\partial t} = -\nabla \cdot \left(\rho \mathbf{v} \mathbf{v} + \mathbf{I} P \right) - \nabla \cdot \left(\mathbf{I} \frac{B^2}{2} - \mathbf{B} \mathbf{B} \right), \quad (2.2)$$

$$\frac{\partial W}{\partial t} = -\nabla \cdot \left(\mathbf{v}(W+P) \right) - \mathbf{v} \cdot \nabla \cdot \left(\mathbf{I} \frac{B^2}{2} - \mathbf{B} \mathbf{B} \right), (2.3)$$

and

$$\frac{\partial \mathbf{B}}{\partial t} = \nabla \times (\mathbf{v} \times \mathbf{B}). \tag{2.4}$$

The variables have their usual meanings: t is time, ρ and P are the plasma density and thermal pressure, \boldsymbol{v} and \boldsymbol{B} are the velocity and magnetic field vectors, respectively,

and ${\bf I}$ is the identity matrix. The energy W is defined as

$$W = \frac{1}{2}\rho v^2 + \frac{P}{\gamma - 1},\tag{2.5}$$

for the ratio of specific heats, $\gamma = 5/3$. The model ignores heat flux and wave pressure in the energy equation. A complete description of the numerical method of solving these equations can be found in Zhang et al. (2019).

2.2. Coordinate Systems

The native output of the GAMERA code is an irregularly gridded Cartesian data set. After each simulation, we perform a coordinate transformation to the spherical expression of the HelioCentric Inertial (HCI) coordinate system. In the HCI system (Fränz & Harper 2002), the XY-plane (0° latitude) is aligned with the solar equatorial plane observed at 2000-01-01 12:00 UTC, the X-axis (0° longitude) points towards the solar ascending node on the ecliptic of J2000.0, and the Z-axis $(+90^{\circ} \text{ latitude})$ points along the solar rotation axis. The RTN spherical system used below to describe the simulation results (Fränz & Harper 2002) is a local coordinate frame where R is the Sun-to-spacecraft direction, T is the toroidal direction obtained when the Sun's spin rotation axis is crossed with R, and N completes the right-handed system. Here we use spherical coordinates r, theta, phi (radius, colatitude, longitude), where solar north is $\theta = 0$ and the equator is $\theta = \pi/2$, where appropriate. To be consistent with in-situ notation, we use R, T, N is for in-situ and modeled in-situ data. In these coordinate systems, R is interchangeable with r. In this paper, we will use spherical coordinate subscripts r, θ, ϕ to denote quantities at radii less than or equal to the radius of the GAMERA inner boundary, and R, T, N to subscript variables modeled by GAMERA.

2.3. Initial and Boundary Conditions

For this study, we examine Carrington rotation 2258 (CR2258; 2022 May 28 – 2022 Jun 24), which included the period of Parker Encounter 12 from 2022 May 27 to 2022 June 7. Figure 1 shows the trajectories of Earth, Parker, and SolO during this time, along with synoptic maps of AIA 193 Å and HMI observations from SDO. The HMI map was downloaded from the Joint Science Operations Center (JSOC; http://jsoc.stanford.edu/) while the AIA map was generated by using 55 full-sun maps (~12 hr cadence). For each AIA image, we applied a Gaussian filter with a full width at half maximum of 7.8 degrees centered on the central meridian. Then, we reprojected each filtered image into the heliographic (Carrington) coordinate frame and summed the intensities.

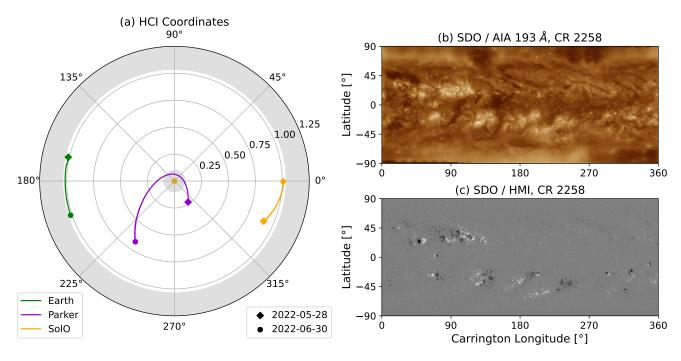


Figure 1. Overview of the modeled time period. Panel (a) shows the trajectories of Earth, Parker, and Solar Orbiter during the time frame, and (b) and (c) show, respectively, synoptic maps of AIA 193 Å and HMI observations from SDO. In (a), white/gray indicates regions inside/outside our computational domain (see Section 2).

In this study, we employ synchronic maps from two photospheric flux transport models to populate the input magnetic field map for CR2258: the ADAPT and AFT models. ADAPT is based on the Worden & Harvey (2000) flux transport method and uses data assimilation techniques to incorporate data from new magnetograms. Measurements near the central meridian (limb) are given the most (least) weight since they are the most (least) reliable. AFT also uses data assimilation to incorporate magnetic data, but while ADAPT typically only assimilates data within 60° from disc center, AFT assimilates data from the input magnetogram to within 3 pixels of the limb. ADAPT also includes the effect of random flux emergence. Both models include differential rotation and meridional flow. AFT uses the observed meridional flow and differential rotation measured by Hathaway et al. (2022), whereas the ADAPT meridional flow profile takes the form given by Wang & Sheeley (1994) and is tuned so that the model reproduces the polar field evolution. Both models incorporate motions representative of the convective flows in some way. ADAPT uses a stochastic diffusion method to mimic the supergranular motions (Simon et al. 1995). In contrast, AFT models the surface flows using vector spherical harmonics to create a convective velocity field that reproduces the characteristics (e.g., size, lifetimes, velocities) of the convective flows observed on the Sun (Hathaway et al. 2010; Ugarte-Urra et al. 2015).

Both models are steady-state in our simulations, meaning that the input map does not get updated during the simulated time period. Improving this assumption will be the subject of future work.

To model the solar wind in the inner heliosphere, GAMERA requires inner boundary conditions at some height, set here to be 0.1 AU or $21.5~R_{\odot}$. In previous studies, these have been provided by the empirical Wang-Sheeley-Arge (WSA; Wang & Sheeley 1990; Arge & Pizzo 2000) coronal model based on ADAPT input magnetic fields (Mostafavi et al. 2022), but in principle can be provided by, for example, WSA based on AFT input, or even by a full MHD model of the low corona (e.g.; Lionello et al. 2014; van der Holst et al. 2014). Our implementation of WSA in this paper can use either ADAPT or AFT as the photospheric boundary condition.

The WSA model relies on a coronal magnetic field, modeled by a PFSS extrapolation solution of a Carrington map of the photospheric magnetic field into the corona to a height of typically a few R_{\odot} . The PFSS solution (Altschuler & Newkirk 1969) assumes that the low corona is current free between the photosphere (where the radial magnetic field is measured directly) and the 'source surface' at $R_{ss}=2.5~R_{\odot}$ (where the field is assumed to be purely radial). The field is then extrapolated from the source surface to 0.1 AU with a SCS model. The SCS solution (Schatten 1971) assumes the

corona outside R_{ss} is current-free between the source surface and infinity, except for a heliospheric current sheet (HCS) separating the positive and negative polarities of the radial magnetic fields. The description of our implementation of the PFSS and SCS solution can be found in Appendix A-Appendix C.

We obtain the distribution of the radial velocity in the inner heliosphere via an empirical formula from WSA that uses information on the expansion of the magnetic field flux tubes between the photosphere and the source surface, and their proximity to the coronal hole boundary on the photosphere (Arge & Pizzo 2000). Together, the PFSS, SCS and the WSA velocity relationship create a model of the magnetic field and velocity from the photosphere into the inner heliosphere, and the inner boundary condition of GAMERA can be extracted from a slice from this solution at some radius, chosen here to be 0.1 AU. The remaining MHD variables at the inner boundary condition are obtained as will be described below, in Equation 2.13-Equation 2.14.

Before initialization of the GAMERA simulation, the coronal model output at the inner boundary of GAM-ERA at arbitrary resolution is interpolated to the GAM-ERA inner boundary grid, also with arbitrary resolution. To account for the solar rotation, at each time step during the simulation, the boundary conditions (radial and toroidal components of the magnetic field, radial component of the velocity, the density, and the temperature) are interpolated to the inertial GAMERA inner boundary grid according to an angular velocity determined by a latitudinally constant (in the simulation) sidereal rotation period of $T_s = 25.38$ days (Merkin et al. 2011), corresponding to a solar latitude of about 26° (sidereal rotation is the time it takes for the Sun to make a single revolution around its axis of rotation relative to the background stars; Roša et al. 1995). In GAMERA, rigid rotation of the corona is assumed out to $21.5R_{\odot}$.

Figure 2 shows the photospheric input field using the two models, as well as B_r and v_r at the inner GAM-ERA boundary R_{in} . The maps are synchronic, meaning they represent a single instant in time, with far-side information updated to that instant in time according to the ADAPT and AFT models. For this study, we use an ADAPT map produced at 2022-06-10 20:00 UT from the Global Oscillation Network Group (GONG) line-of-sight (LOS) data (Harvey et al. 1996). The AFT map from 2022-06-10 at 16:00 UT was made using SDO/HMI LOS data. In both cases, the LOS component of the magnetic field was divided by the cosine of the angle from the disk center to approximate the radial magnetic field (Upton & Hathaway 2014). These dates and times are slightly

before the midpoint of CR2258 on 2022-06-10 21:21 UT, and were chosen because GAMERA assumes that the Earth is at 180° Carrington longitude at t=0. The ADAPT model typically scales input magnetograms by an overall constant whose value depends on each magnetograph (Barnes et al. 2023), which can vary over time depending on instrumental upgrades. The scaling is applied to match the photospheric flux to that measured by Kitt Peak Vacuum Telescope (C. Henney, personal communication). This scaling is, therefore, different for each magnetograph, since the strength of the magnetic field that these measure can be significantly different (Virtanen & Mursula 2017). AFT does not natively perform this scaling, so the photospheric AFT map used in this study, shown in Figure 2, has been multiplied by a factor of 1.58 to obtain the same net unsigned photospheric flux as in the ADAPT map.

The maps at R_{in} (middle panels) are created by performing a PFSS extrapolation of CR2258 using the ADAPT/AFT maps to R_{ss} , and then calculating the SCS model (Appendix C) and extracting the magnetic field components at R_{in} . We initialize our v_r inner boundary conditions at R_{in} from the WSA velocity equation applied to the PFSS extrapolation of CR2258. In principle, R_{in} can be reduced somewhat to capture regions closer to the Sun, but the inner boundary conditions of the inner heliospheric model, which assume no radially inward characteristics imply that flows slower than the fast magnetosonic speed, such as those occurring closer to the Sun, will produce numerical, nonphysical artifacts at the boundary, preventing R_{in} from being placed arbitrarily close to the Sun. At the inner boundary, the initial radial velocity in WSA is given by (e.g., Arge & Pizzo 2000; Wallace et al. 2020, 2021):

$$v_r = V_{sw} + \frac{V_{fw}}{(1+f_s)^{2/9}} \left(1 - \frac{4}{5} \exp\left(-(d/2)^2\right)\right)^3$$
 (2.6)

where $V_{sw} = 285 \text{ km s}^{-1}$ and $V_{fw} = 625 \text{ km s}^{-1}$, and f_s and d are, respectively, the coronal magnetic flux tube expansion factor and the shortest angular distance (in degrees, calculated in the heliocentric coordinate system, described below) to the nearest coronal hole boundary at the photosphere. The expansion factor is defined as the scaled ratio of the total magnetic field magnitude at the photosphere and source surface and is given by the equation (Wang & Sheeley 1990):

$$f_s = \left(\frac{R_{\odot}}{R_{ss}}\right)^2 \left(\frac{B_{ph}}{B_{ss}}\right). \tag{2.7}$$

Since magnetic flux is conserved, a self-similarly expanding flux tube has $f_s = 1$, while an over (under) expanding flux tube has f_s greater than (less than) one. We

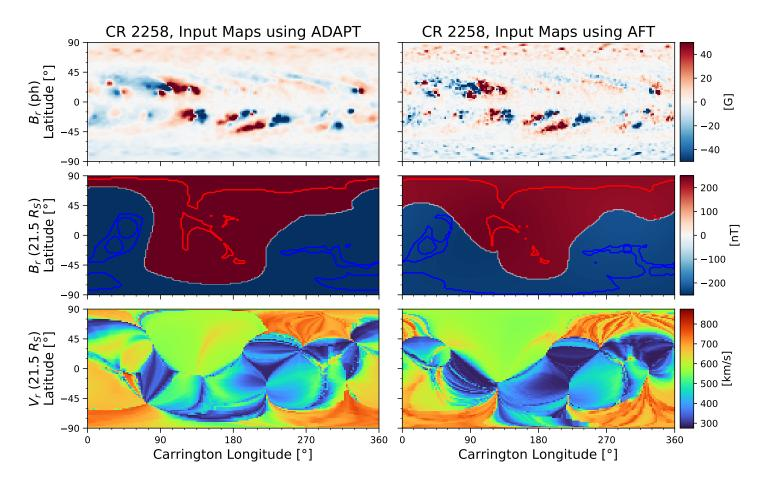


Figure 2. Synchronic maps from the ADAPT (left) and AFT (right) models. The top panels show the photospheric radial magnetic field. The middle and bottom panels show the radial magnetic field and radial velocity, respectively, at the inner GAMERA boundary. These are obtained by extrapolation via a PFSS solution to the source surface followed by a SCS model out to the inner boundary. In the middle panels, red/blue lines indicate contours of open flux at the photosphere overplotted on color scale B_r at $21.5R_{\odot}$.

calculate f_s and d at the photosphere, then obtain v_r from Equation 2.6 by tracing field lines from R_{in} to R_{ss} and then transfer v_r out to R_{in} by assuming these are constant on field lines. The remaining velocity components at R_{in} are given by

$$v_{\theta}(R_{in}, \theta, \phi) = 0, \tag{2.8}$$

and

$$v_{\phi}(R_{in}, \theta, \phi) = 0, \tag{2.9}$$

in the inertial frame used by GAMERA. Finally, the remaining magnetic field components at R_{in} are given by

$$B_{\theta}(R_{in}, \theta, \phi) = 0, \tag{2.10}$$

$$B_{\phi}(R_{in}, \theta, \phi) = \frac{\Omega R_{in} \sin \theta}{v_r(R_{in}, \theta, \phi)} B_r(R_{in}, \theta, \phi), \quad (2.11)$$

where

$$\Omega = 2\pi/T_s. \tag{2.12}$$

The initial density is specified using an empirical relationship with the radial velocity, obtained by fitting the Helios data (McGregor 2011; Merkin et al. 2016) as follows:

$$n = 112.64 + 9.49 \times 10^7 / v_r^2,$$
 (2.13)

for velocity measured in km s⁻¹ and density $(n = \rho/m_p)$ for m_p the proton mass) in cm⁻³. The initial solar wind temperature is derived assuming a balance of the total pressure (a sum of the thermal pressure and the magnetic pressure) at R_{in} according to:

$$nk_BT + \frac{B_r^2}{8\pi} = n_{HCS}k_BT_{slow},$$
 (2.14)

where k_B is Boltzmann's constant. The right-hand side of the equation is a constant corresponding to the pressure in the HCS, where the magnetic pressure component is negligible. Following Mostafavi et al. (2022), n_{HCS} is the maximum number density in the HCS at

 R_{in} , and $T_{slow} = 3.6 \times 10^5$ K is a representative temperature of the slow wind, in line with Helios measurements (Sanchez-Diaz et al. 2016).

In this simulation, the grid setup is similar to the previous GAMERA- and LFM-studies referred to in Section 2.1. A uniform spherical grid is used in the simulation domain extending from $R_{in} \leq r \leq 220~R_{\odot}$ in the radial direction, $18^{\circ} \leq \theta \leq 162^{\circ}$ in the colatitudinal direction ($\theta = 0^{\circ}$ corresponds to the solar north), and $0 \leq \phi \leq 360^{\circ}$ in the longitudinal direction. The grid resolution used in this study is $N_r \times N_{\theta} \times N_{\phi} = 256 \times 128 \times 256$ leading to the cell size $\Delta r \times \Delta \theta \times \Delta \phi = 0.78 R_{\odot} \times 1.1^{\circ} \times 1.4^{\circ}$.

The plasma variables in the simulation volume are obtained by assuming that for the initial state of the simulation volume $B_r(r)$ falls off from the inner boundary as r^{-2} , and the radial velocity, density, and temperature are all constant with radius, with values determined at the inner boundary of GAMERA. This causes the solar wind to blow out and equilibrate the initially uniform heliosphere over the course of about 200 hours. Following this 'negative time', at simulation time t=0, the ϕ placement of the Earth relative to the Sun is such that it will be oriented at $\phi=\pi$ at the central time of the Carrington map.

3. RESULTS

We plot snapshots of the heliospheric variables in Figure 3, where we show $\log(R^2n)$, R^2B_R and v_R in the equatorial slice of GAMERA simulation output for both the ADAPT and AFT photospheric model inputs at a time near the closest approach of Parker to the Sun. Hereafter, these will be referred to as GAMERA/ADAPT and GAMERA/AFT to differentiate them from the purely WSA treatment based on the ADAPT and AFT maps, which will be called WSA/ADAPT, WSA/AFT. In the plot, R is the radial coordinate between the Sun and each satellite. The perihelion itself (13.3 R_{\odot} for Encounter 12) was not captured by our GAMERA runs because it was inside R_{in} , though this is not crucial for testing the fidelity of our model. We choose this scaling for our plots because radial magnetic and mass flux are expected to be constant, so B_R and n will scale as R^{-2} , assuming v_R is approximately constant with R.

We obtained the position of various spacecraft and Earth at each time step using the SpiceyPy (Annex et al. 2020) and Astropy (The Astropy Collaboration et al. 2018) packages. The state variables obtained by solving Equation 2.1-Equation 2.4 were then linearly interpolated from the 8 nearest grid points to the local position of each satellite while field lines were traced

from the location of each satellite using a fourth-order Runge-Kutta solver, solving the field line equations in spherical coordinates:

$$\frac{dr}{ds} = \frac{B_r}{|\mathbf{B}|}$$

$$\frac{d\theta}{ds} = \frac{1}{r} \frac{B_{\theta}}{|\mathbf{B}|}$$

$$\frac{d\phi}{ds} = \frac{1}{r \sin \theta} \frac{B_{\phi}}{|\mathbf{B}|}.$$
(3.1)

We used fixed stepsizes of $ds = 10^{-3}R_{\odot}$ to obtain the positions (r_i, θ_i, ϕ_i) of successive points i along the field line originating at each satellite at each time step. The endpoint location of the field line at each time step on the inner boundary was identified and mapped back down to its source region via the corresponding coronal magnetic field model.

3.1. In-situ Measurements

The in-situ solar wind data was obtained from the science-grade observations available through NASA's CDAWeb data repository. For most of Parker's orbit, we use level-3 plasma moments from the SPC instrument (Case et al. 2020), since it has the best overall cadence and quality. Unfortunately, however, SPC has saturation and field-of-view issues near perihelion (c.f. the data release notes). Therefore we fill in the missing data inside 22 R_{\odot} using level-3 plasma moments from the SPAN-I instrument (Livi et al. 2022), which has the opposite problem (i.e. good data near perihelion, but poor field-of-view and statistics further out). Throughout the entire Parker orbit, we use 1-minute magnetic field data from the MAG instrument in the FIELDS suite (Bale et al. 2016). At SolO, we use bulk plasma data from SWA-PAS (Louarn et al. 2020) and 1-minute magnetic field observations from the MAG instrument. At Earth, we use both plasma and magnetic field data from the hourly OMNI database (Papitashvili & King 2020) which aggregates data from multiple near-Earth spacecraft and time-shifts the data to the Earth's bow shock. For this time period, the OMNI data is based on plasma data from Wind / SWE (Ogilvie et al. 1995) and magnetic field measurements from Wind / MFI (Lepping et al. 1995). The data at all locations were resampled to a cadence of 2.5 hours by applying a boxcar average to only the data with "good" quality flags.

Figures 4-6 show a comparison between the measured and GAMERA/ADAPT and GAMERA/AFT model insitu data at Parker, SolO and Earth. For each time series, we overplot the GAMERA/ADAPT and GAMERA/AFT model predictions as black and red curves, respectively, as well as the associated SCS magnetic field

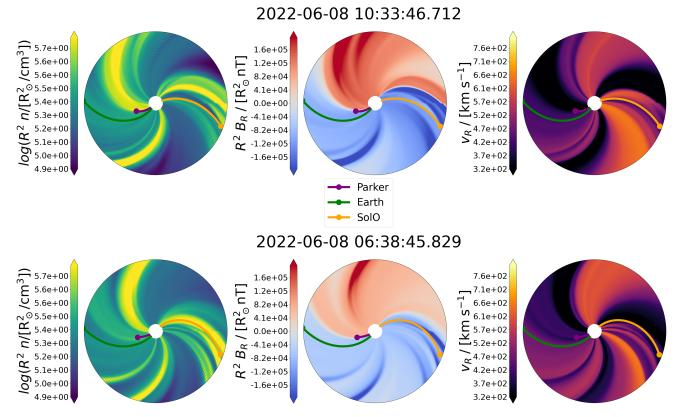


Figure 3. Equatorial cuts of density (left), B_R (center), and v_R (right) from the GAMERA simulations using the ADAPT (top) and AFT (bottom) models. Field lines connecting the spacecraft and Earth to the inner boundary are projected onto the equatorial plane.

data for times when Parker is below R_{\odot} . Time periods including interplanetary CMEs (ICMEs; these directly hit the spacecraft) in the HELIO4CAST catalog (Möestl et al. 2023) are marked in the shaded red regions.

For each satellite, the plot of v_R also includes a prediction from WSA/ADAPT or WSA/AFT (Arge & Pizzo 2000), which applies a constant radial velocity between $21.5R_{\odot}$ and 1 AU to each plasma parcel originating at $21.5R_{\odot}$ (where the velocity was obtained via Equation 2.6). At increments of 1/10 AU, stream interaction regions modify this velocity via

$$v_R(R) = \sqrt{2} \left[\left(v_R(R) \right)^{-2} + \left(v_R(R + dR) \right)^{-2} \right]^{-1/2}, (3.2)$$

such that plasma parcels moving faster than the parcels ahead of them are slowed down. The polarity of the magnetic field assigned to each parcel is kept constant throughout space, allowing the sign of the magnetic field to be obtained at each satellite from WSA/ADAPT or WSA/AFT. We did not find significant differences in the results if this model used Equation 3.2 as opposed to assuming a constant velocity between R_{in} and 1 AU.

The shaded region seen near 01 Jun is due to the trajectory of Parker being inside R_{in} , so we use the magnetic field obtained from the SCS layer of the model in this region. For Parker, the general behavior of the radial and transverse magnetic field data is reproduced reasonably well with both GAMERA/ADAPT and GAMERA/AFT models. Furthermore, although Parker is inside the inner boundary of our simulation near 01 Jun, the SCS layer of the models reproduce the first HCS crossing, as does the inferred polarity from the WSA models. Both MHD models capture the second and third HCS crossings, with GAMERA/ADAPT capturing the timing of the HCS crossing slightly better than GAMERA/AFT, while the inferred WSA/ADAPT and WSA/AFT polarities lags. B_N is always close to 0 in the GAMERA model since it is set to near 0 by the initial conditions and the only new B_N results from the v_N component of Equation 2.4 generated by Parker being slightly out of the equatorial plane. (Mostafavi et al. 2022) also find a small nonzero v_N generated near stream interaction regions. The rest of the model's variables are qualitatively hard to compare against the in-situ measurements due to the number of data gaps. The model velocity structure has some regions of overlap with the in-situ data, but generally shows high speed solar wind throughout the time interval, even where the in-situ

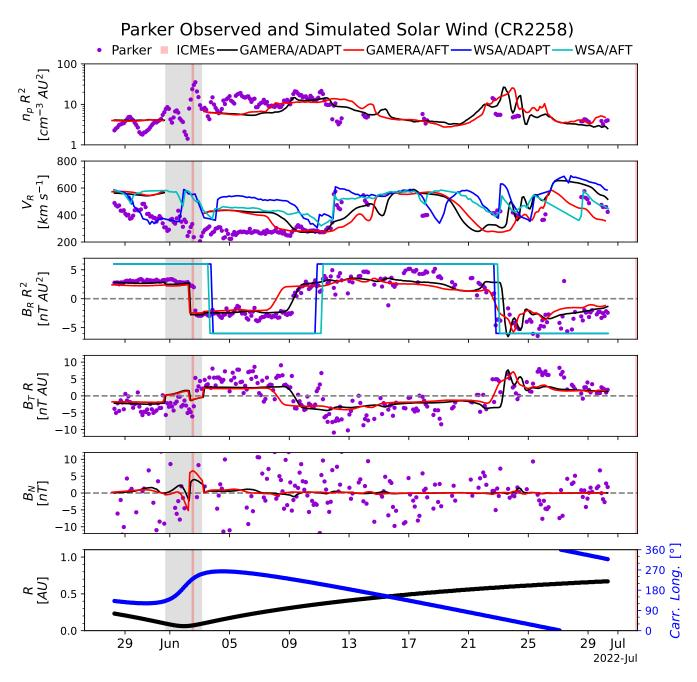


Figure 4. Comparison of the measured in-situ data at Parker with the in-situ data from both GAMERA models. Density, v_R , B_RR^2 , B_TR , B_N , and distance from the Sun's center (R) and Carrington longitude are plotted from top to bottom. ADAPT/AFT data is shown in black/red. The measured in-situ data was averaged onto the simulated 2.5 hr cadence. The shaded region near 01 Jun corresponds to the time interval when Parker was inside R_{in} , so the magnetic field values there are taken directly from the SCS layer of the coronal model. The radial velocity and magnetic field polarity from WSA/ADAPT and WSA/AFT are also shown for each case. Shaded red regions are time intervals with ICMEs measured by Parker.

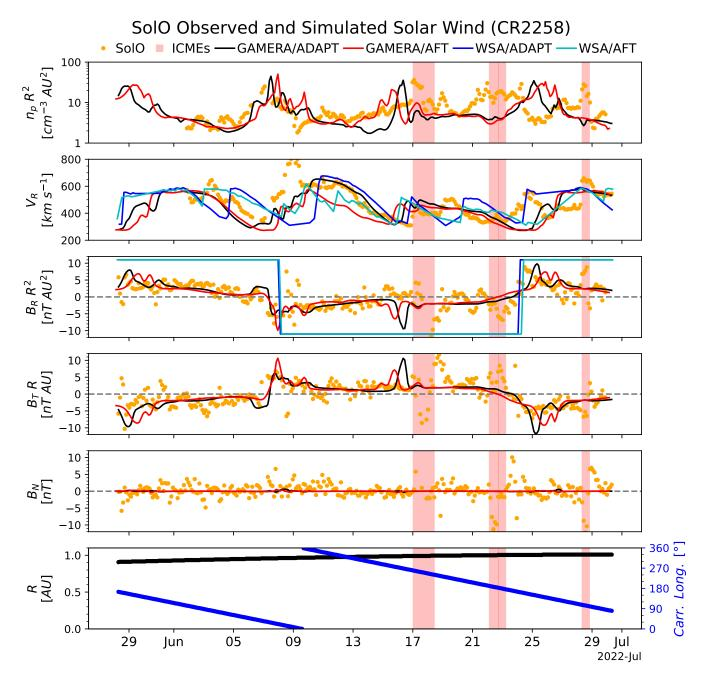


Figure 5. Same as Figure 4 but for SolO.

measurements show slow wind. A statistical analysis of the extant data (described below) does not show good agreement for density or radial velocity.

The same comparisons for SolO and OMNI data are shown in Figure 5 and Figure 6, respectively. The MHD models seem to capture much of the qualitative behavior of the in-situ data. Qualitatively, the purely WSA predictions seem to perform worse than the MHD predictions at SolO, and comparably at Earth. At SolO, in particular, the MHD models seem to capture the cross-

ings of the HCS a bit better than pure WSA, and reproduce the velocity better.

We quantify the fit between our models and the in-situ data from each satellite by examining the Pearson coefficient between the simulated and observed plasma variables. In Figure 7 we show the observed and simulated n_p , v_R , B_R and B_T values for Parker (top row), SolO (middle row), and OMNI (bottom row). Results from the GAMERA/ADAPT run are plotted with black "x's" while results from the GAMERA/AFT run are plotted

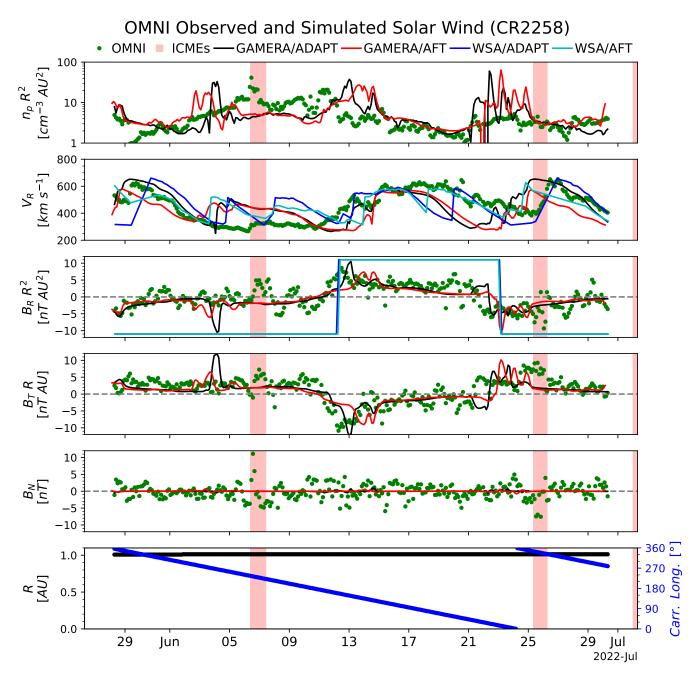


Figure 6. Same as Figure 5 but for Earth.

with red crosses. In addition, the third column shows the radial velocity predicted using the WSA/ADAPT and WSA/AFT models (Equation 3.2). These plots exclude the data during the interval when ICMEs were present, as our steady state model is not expected to reproduce the data during this time period. The results show that the MHD models perform best at matching Parker radial magnetic field data, with a Pearson $r_{XY} \sim 0.86$. The radial magnetic field data is reasonably well reproduced at SolO ($r_{XY} \sim 0.54$) and Earth

 $(r_{XY} \sim 0.63)$, but the density $(r_{XY} \sim 0.1)$ is not. The radial velocity at all three locations is somewhat poorly reproduced by the MHD models $(r_{XY} \sim 0.4-0.5)$, but WSA/ADAPT and WSA/AFT perform comparably or worse $(r_{XY} \sim 0.1)$ in all three cases. We also performed a phase offset study to see if shifting the model data in time by some arbitrary amount to the left or right (backward or forward in time) would be a better fit to the in-situ measurements, but the results indicated that the phase offset that maximized the Pearson coefficient

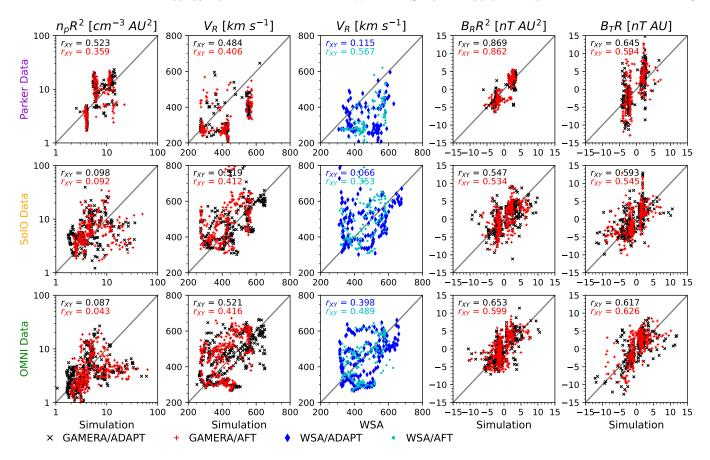


Figure 7. Scatter plots comparing the observed and simulated n_p , v_R , B_R and B_T values for Parker (top row), SolO (middle row), and OMNI (bottom row). Black "x's" show the comparison for GAMERA/ADAPT results and red crosses show the GAMERA/AFT results. The third column shows the WSA/ADAPT and WSA/AFT model results for the radial velocity. In each plot, r_{XY} denotes the sample Pearson correlation coefficient for each set of points.

was at most a few hours in all cases, and did not make a noticeable difference in the quality of the correlation.

An additional feature of these quantitative comparisons is that the simulated radial velocity seems to be uniformly overpredicted at Parker but not at SolO or Earth. One possible explanation for this is that there is residual acceleration of the solar wind that happens past Parker (Dakeyo et al. 2022) that is not accounted for in WSA, which has fine-tuned its parameters for 1 AU.

3.2. Magnetic Connectivity

The magnetic connectivity of the satellites to the photosphere can be tracked throughout the simulation in one of two ways. Either (1) ballistically (Badman et al. 2020), where the ϕ position of the footpoint at $r = R_{\odot}$ is calculated at constant θ via

$$\phi(r = R_{\odot}) = \phi - \frac{180\Omega}{\pi v_R(r)} \Big(R_{\odot} - r \Big), \qquad (3.3)$$

or (2) directly, by tracing magnetic field lines as described above, from the satellites to the inner boundary

of GAMERA, whereupon the connectivity to the photosphere is determined by tracing the field lines through the SCS and PFSS solutions. Using these methods, we can obtain the modeled photospheric footpoint of the magnetic field line connected to each satellite at each time step.

We plot the locations of these footpoints calculated from method (2) for SolO in Figure 8. The footpoints are clearly seen to connect to the modeled open field areas (red and blue contours) in both the ADAPT and AFT maps, though these open field regions do not always coincide with the dark EUV emission areas (white contours) identified in the AIA 193 Å images with the EZSEG algorithm (Caplan et al. 2016), which uses an image segmentation technique combined with a simple region-growing algorithm. The mismatch between the bright regions and open field regions can sometimes result from bright coronal loops in the vicinity masking small coronal holes. The ballistic mapping footpoints are not quantitatively different from those obtained by direct tracing, in agreement with the finding that foot-

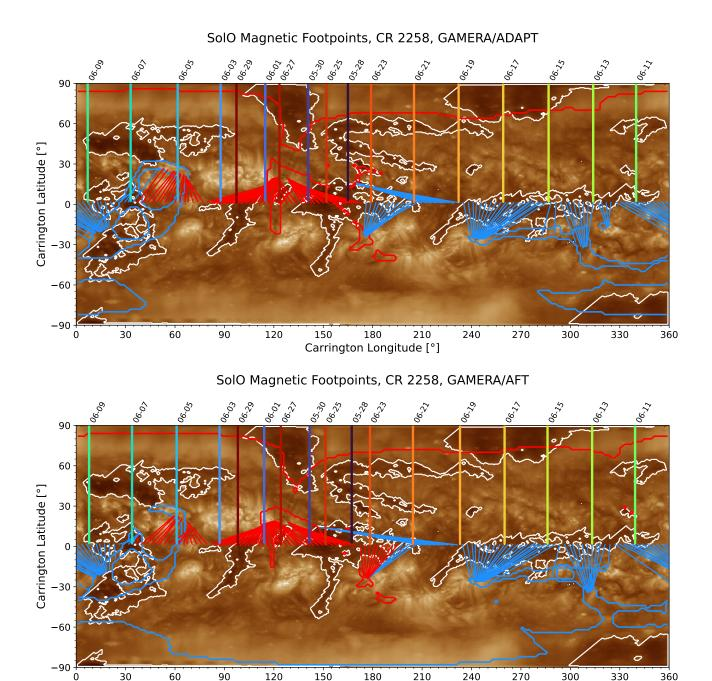


Figure 8. The photospheric footpoints of the field lines connecting to SolO from both GAMERA models are overplotted on the associated synoptic AIA maps. Color shading of the thick vertical lines represents time, and the thin straight lines starting near 0° latitude originate at the location of SolO and connect down to the photosphere. Although the field lines follow a curved trajectory, only the start and end points are shown, connected by a straight line, since the actual trajectory is hard to discern for so many field lines. The red/blue contours encircle open flux of positive/negative polarity on the photosphere based on the associated ADAPT-PFSS and AFT-PFSS extrapolations. The measured in-situ sign of B_R is coded on this plot in the color of the field lines. White contours indicate coronal holes identified using the EZSEG algorithm.

Carrington Longitude [°]

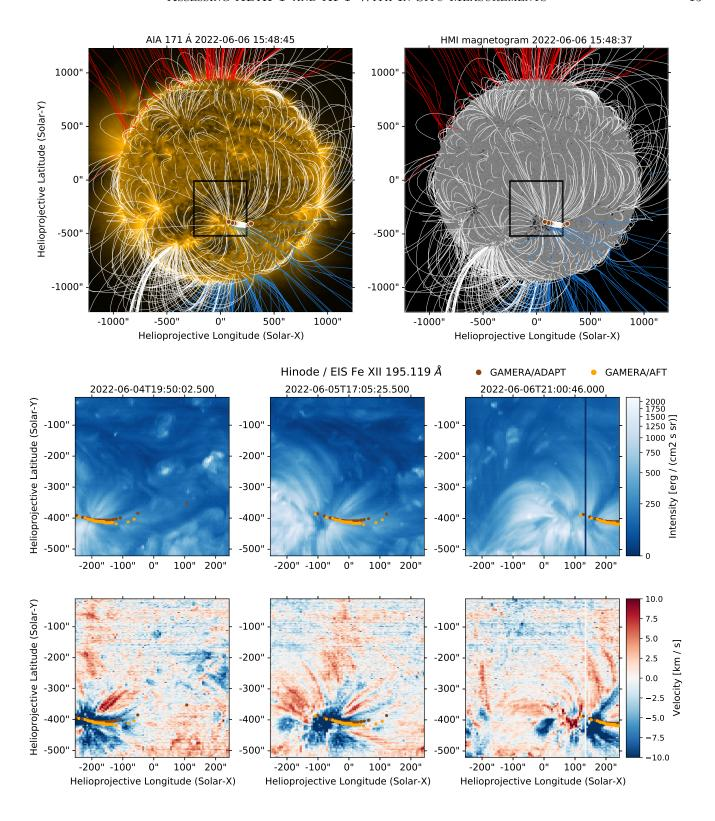


Figure 9. Top panels: PFSS field lines, calculated using a full-sun synoptic map, plotted on an AIA 171 Å image and HMI line-of-sight magnetogram. Closed field lines are shown in white. Open field lines are shown in red (positive) and blue (negative). The black box shows the EIS field of view. In the helioprojective coordinate system (Thompson 2006), the Cartesian variables X and Y correspond, respectively, to the longitude and latitude measured relative to the center of the observed solar disk. Middle panel: Intensity and Bottom panel: Doppler velocity measured by EIS in the Fe XII 195.119 Å line at three times during this interval. The orange/brown dots shown are footpoints connected to SolO rotated to the time of the EIS raster from the ADAPT/AFT MHD models. In the bottom panel, Red/blue indicates a downflow/upflow. This convention, where velocities toward the observer are blue shifted with negative values, effectively reverses the direction of positive velocity with respect to the rest of the paper. We keep this standard convention in this Figure, and note that the negative velocity values here correspond to outflows away from the Sun.

point mapping is consistent across different combinations of coronal and heliospheric models (Badman et al. 2022). Occasionally the polarity of the traced field lines does not match the polarity of their source regions, as, for example, around 5 June and 23 June.

During the time period 18–24 June 2022, both direct and ballistic connectivity models show that SolO was magnetically connected to an active region on the photosphere. We compare the locations of the photospheric footpoints traced from SolO against Doppler maps obtained from spectroscopic observations of the upper solar atmosphere, measured by calculating the Doppler shift along the line of sight in the Fe XII line measured with EIS. There have been many observations of active region outflows with EIS that are suggestive of a connection to the solar wind (e.g., Sakao et al. 2007; Del Zanna 2008; Doschek et al. 2008; Brooks & Warren 2011; Brooks et al. 2015; Harra et al. 2021). As is illustrated in Figure 9, the GAMERA/ADAPT and GAMERA/AFT field lines connecting SolO to the solar surface suggest that the solar wind it measures during the period of 14-19 June 2022 originated in an active region outflow since there is a blue-shifted (negative velocity) plage region at the footpoints of magnetic field lines connected to SolO from both simulations. Although in this case there are open field lines associated with the outflow region, this is not universally true, as some outflows are in regions where a PFSS model shows closed field (e.g., Culhane et al. 2014). It is not clear if, in these cases, the PFSS is a poor representation of the magnetic topology or if the outflows are siphon flows on long, closed field lines.

If the solar wind observed by SolO during 14–19 June 2022 originated in or near an active region, we would expect some signatures in the charge states and abundance ratios of heavy ions (e.g., He, C, O, Fe). In particular, we should expect to see higher O^{7+}/O^{6+} ratios, indicative of a hotter source region, and abundance ratios closer to coronal values than photospheric (Owocki et al. 1983). Figure 10 shows a closer view of solar wind observed at SolO for 14-27 June. The top three panels show the bulk solar wind density and radial velocity measured by SolO's SWA-HIS, and radial magnetic field measured by the MAG instrument, along with the corresponding simulation results, while the fourth and fifth panels show the O^{7+}/O^{6+} and Fe/O heavy ion ratios measured by the SWA-PAS (Louarn et al. 2020; Owen et al. 2020). The dashed line at 0.145 in the O^{7+}/O^{6+} panel roughly separates coronal hole (< 0.145) and non coronal hole (≥ 0.145) type wind (Zhao et al. 2009). The dotted grey line in the Fe/O panel is a reference coronal value of 0.18 from Feldman (1992) and the two dashed red lines are photopsheric values for Fe/O of 0.069 and 0.047 from Asplund et al. (2009) and Grevesse & Sauval (1998), respectively. Although several ICMEs passed SolO during this time period, there is, nevertheless, evidence of an increase in the heavy ion ratios of O^{7+}/O^{6+} and Fe/O over their reference (dashed line) values. While not definitive, this does provide evidence that SolO was, indeed, connected to an active region at this time.

4. DISCUSSION

In this paper, we presented the results of a comparison between heliospheric modeling using the ADAPT and AFT surface flux transport models. For both ADAPT and AFT maps for CR2258, we used a WSA velocity equation coronal model to initialize a GAMERA MHD heliospheric model. We compared the output of these models to in-situ data from Parker, SolO, and OMNI, and quantitatively compared the performance of GAM-ERA/ADAPT to GAMERA/AFT. We found that the models performed similarly in all cases, and that if one model matched (did not match) the in-situ data, the other model also matched (did not match). The models did best at matching the radial magnetic field at Parker, and did poorly at matching the radial velocity at all three satellites. The MHD simulations performed comparably to a purely WSA model at matching the radial velocity at Parker and Earth, but somewhat better at SolO. Finally, we performed a connectivity analysis to determine that SolO was magnetically connected to an active region observed by Hinode/EIS, and on-board instruments on SolO measured increased heavy ion ratios during this time, potentially indicating a hotter, AR, coronal, rather than cooler, coronal hole, photospheric, source region.

Our work represents two novel additions to the literature. First, to our knowledge, this is the first coronal+heliospheric model to be performed using AFT. Previous work has used AFT to predict polar fields and the solar cycle (Upton & Hathaway 2018) or tested ADAPT against other surface flux transport models (Schrijver & Title 2001) and found large differences when a new active region appeared in the assimilation window (Barnes et al. 2023). However, this study assesses how well AFT performs as the input for coronal and heliospheric modeling relative to the industry standard of ADAPT, and finds that AFT performs just as well. Second, this is the first study, to our knowledge, that has attempted to reproduce in-situ SolO measurements using any coronal or heliospheric model. An intriguing result is the comparison between the WSA prediction of the velocity and the in-situ measurements at SolO. Given that SolO is nearly at 1 AU and very close to

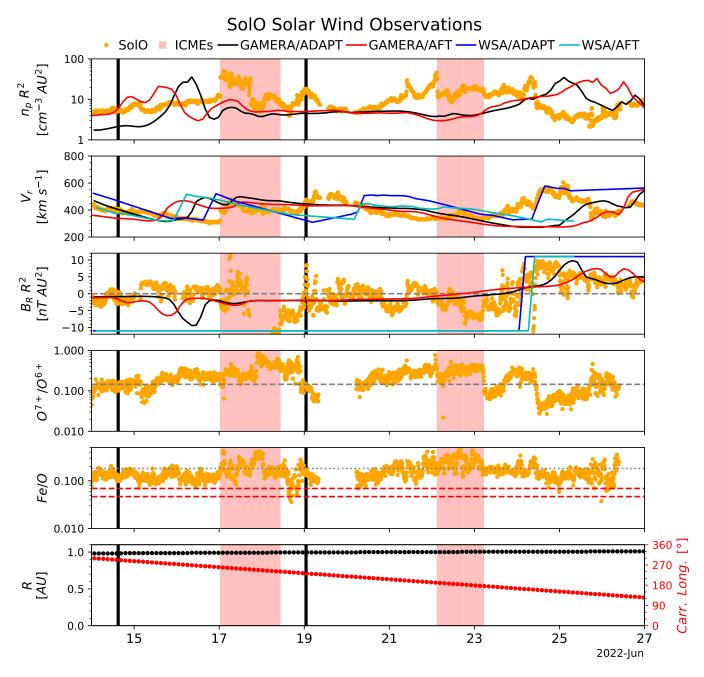


Figure 10. Bulk solar wind observed by SolO / SWA-PAS $(n_p \text{ and } v_R)$, MAG (B_R) , and heavy ion ratios from SWA-HIS $(O^{7+}/O^{6+} \text{ and } Fe/O)$. The black, vertical lines indicate the boundaries of the time range when SolO is thought to be connected to an active region. The dashed line in the O^{7+}/O^{6+} panel indicates a reference value of 0.145, which roughly separates hotter, coronal source regions (≥ 0.145) from cooler, photospheric ones (< 0.145; Zhao et al. 2009). The dotted gray line in the Fe/O panel is a reference coronal value of Fe/O = 0.18 from Feldman (1992) and the two dashed red lines correspond to photopsheric values of Fe/O = 0.069 and 0.047 from Asplund et al. (2009) and Grevesse & Sauval (1998), respectively.

the equatorial plane during this time period, it could be expected that WSA should perform equally well at predicting the solar wind velocity at Earth and SolO. The poor performance of WSA at SolO is therefore somewhat surprising. One possibility is that WSA is correctly calibrated for 1 AU, but the far side magnetogram information is lacking, resulting in poor predictions 180° from Earth, where SolO is situated. Interestingly, the simulated overestimate of the velocity seen at Parker, but not at SolO or Earth, indicates that the parameters of the WSA models, which have been fine tuned for 1 AU, are not appropriate for locations closer to the Sun. While this does seem to demonstrate the smaller velocity of the solar wind near the Sun (Dakeyo et al. 2022), attempts to reset the parameters of WSA based on Parker data have not, thus far, yielded significantly improved results (Samara et al. 2022).

The overall results presented here are in line with previous heliospheric models – both based purely on ballistic or the WSA velocity equation (Arge & Pizzo 2000) and MHD approaches (Kim et al. 2020; Riley et al. 2021), or a mix thereof (Badman et al. 2022) - that steady state models can reproduce in-situ properties at various positions in the heliosphere. Still, our work is the first to examine whether using the AFT flux transport model could improve heliospheric in-situ predictions over those made using ADAPT. Although AFT does not perform better than ADAPT, the fact that it performs comparably is evidence that the treatment of flux transport itself may not be the cause of discrepancies between model and in-situ measurements. Nevertheless, it seems likely that the source of the discrepancies between model predictions and in-situ measurements is in the coronal portion of these models. Eight suspect assumptions made in the coronal portion of our model include (1) The steady-state assumption (the Sun is dynamically evolving) and the lack of accurate far side information, (2) the PFSS assumption (there are very likely currents between the photosphere and R_{ss} , Schuck et al. 2022), (3) the SCS assumption (there is no reason to suppose that all currents above the photosphere are concentrated in a shell at R_{ss} and in the HCS, (4) the WSA velocity assumption (which is an empirical relationship and does not account for mass or momentum conservation), (5) an empirical relationship between the velocity and the density at R_{in} (which again does not account for mass or momentum conservation), (6) the lack of a proper energy treatment, including heat flux and Alfvén wave damping, (7) the lack of time dependence of the boundary conditions, and (8) the lack of solar far-side information. Coronal MHD models avoid many of these assumptions (e.g., Riley et al. 2012; Lionello et al. 2014), and assumption (3) (and potentially 2) seems to be vindicated (though not proven) by the generally good agreement of the model and in-situ magnetic field components, both in the heliospheric portion of the model and in the SCS layer. However, all of these assumptions, and especially the empirical relationships between the magnetic field, velocity, and density, are worth examining further.

Another important takeaway from this work is that using SolO to model the solar wind enables associating in-situ compositional data with the source region on the Sun through the connectivity mapping. Although the results are not definitive, they do seem to be mostly connectivity model independent, indicating that SolO could reliably be used to understand active region and solar wind heating.

Our work does not endeavor to address long-standing problems in heliospheric physics such as the 'open flux problem' (Linker et al. 2017; Arge et al. 2023), the origin of switchbacks (Tenerani et al. 2020; Drake et al. 2021; Pecora et al. 2022), or the source of the slow solar wind (Antiochos et al. 2011; Abbo et al. 2016; Higginson et al. 2017). Nevertheless, the ultimate goal of heliospheric modeling is the accurate and timely prediction of geoeffective events. Future work will attempt to compare different input boundary conditions to determine how optimally to reproduce in-situ data, and compare different models (e.g., Riley et al. 2021; Wu et al. 2020) against each other. Another possibility is to change the parameters of the expansion factor in the WSA model (Wu et al. 2020; Samara et al. 2022) to improve the agreement with the in-situ data. Additionally, including far side information in the photospheric flux transport model (Upton et al. 2019) may be a way to improve the quality of in-situ predictions.

ACKNOWLEDGMENTS

This work was sponsored by the Office of Naval Research 6.1 program (KJK, HPW, MGL, IUU), NASA's Living with a Star program (HPW, IUU, LAU, MGL), NASA's Parker Solar Probe/WISPR program (KJK, MGL), and NASA's Hinode program (MJW, YKK, HPW, IUU). EP acknowledges the support of NRL's contract N00173-22-2-C601. The authors are grateful to Karl Battams, Nicholas Crump, Cooper Downs, Brendan Gallagher, Carl Henney, Peter MacNeice, Slava Merkin, Pete Riley, Roger Scott, Kareem Sorathia, and Yi-Ming Wang for helpful discussions and technical advice. The authors are also grateful to the anonymous referee, whose careful reading of, and comments on, the initial manuscript helped highlight several issues. HPW acknowledges support from ISSI for team 463, "Exploring The Solar Wind in Regions Closer Than Ever Observed Before." We acknowledge the NASA Parker Solar Probe Mission and the SWEAP team led by J. Kasper for the use of data. The FIELDS experiment on the Parker Solar Probe spacecraft was designed and developed under NASA contract NNN06AA01C. Hinode is a Japanese mission developed and launched by ISAS/JAXA, collaborating with NAOJ as a domestic partner, NASA and UKSA as international partners. Scientific operation of the Hinode mission is conducted by the Hinode science team organized at ISAS/JAXA. This team mainly consists of scientists from institutes in the partner countries. Support for the post-launch operation is provided by JAXA and NAOJ (Japan), UKSA (U.K.), NASA, ESA, and NSC (Norway).

APPENDIX

A. POTENTIAL MAGNETIC FIELD INSIDE A SPHERICAL SHELL

We want to solve for a potential magnetic field in a spherical shell, i.e., one that satisfies

$$\nabla \times \mathbf{B} = 0. \tag{A1}$$

The solution is

$$\boldsymbol{B} = -\nabla \Psi. \tag{A2}$$

For a solenoidal magnetic field, Ψ therefore satisfies

$$\nabla^2 \Psi = 0 \tag{A3}$$

whose general solution is, in spherical coordinates (Jackson 1998):

$$\Psi(r,\theta,\phi) = \sum_{l=0}^{\infty} \sum_{m=-l}^{l} \left[A_{lm} r^l + B_{lm} r^{-(l+1)} \right] Y_{lm}(\theta,\phi).$$
 (A4)

The $Y_{lm}(\theta,\phi)$ are spherical harmonics satisfying the orthogonality condition

$$\int_0^{2\pi} d\phi \int_0^{\pi} d\theta \sin\theta \ Y_{l'm'}^*(\theta,\phi) Y_{lm}(\theta,\phi) = \delta_{l'l} \delta_{m'm}. \tag{A5}$$

The components of the magnetic field $B = -\nabla \Psi$ are then:

$$B_r = -\frac{\partial \Psi}{\partial r} = -\sum_{l=0}^{\infty} \sum_{m=-l}^{l} \left[l A_{lm} r^{l-1} - (l+1) B_{lm} r^{-(l+2)} \right] Y_{lm}(\theta, \phi), \tag{A6}$$

$$B_{\theta} = -\frac{1}{r} \frac{\partial \Psi}{\partial \theta} = -\sum_{l=0}^{\infty} \sum_{m=-l}^{l} \left[A_{lm} r^{l-1} + B_{lm} r^{-(l+2)} \right] \frac{\partial Y_{lm}(\theta, \phi)}{\partial \theta}, \tag{A7}$$

$$B_{\phi} = -\frac{1}{r\sin\theta} \frac{\partial \Psi}{\partial \phi} = -\frac{1}{\sin\theta} \sum_{l=0}^{\infty} \sum_{m=-l}^{l} \left[A_{lm} r^{l-1} + B_{lm} r^{-(l+2)} \right] im Y_{lm}(\theta, \phi). \tag{A8}$$

B. THE POTENTIAL FIELD SOURCE SURFACE MODEL

The potential field source surface (PFSS; Altschuler & Newkirk 1969) model solves for the magnetic field $\mathbf{B} = -\nabla \Psi$ inside a region given by $R_1 \leq r \leq R_2$, where the boundary condition at R_1 is the Neumann condition

$$\left. \frac{\partial \Psi}{\partial r}(r, \theta, \phi) \right|_{R_1} = -B_r(R_1, \theta, \phi)\hat{\mathbf{r}},\tag{B1}$$

and the boundary condition at R_2 is the Dirichlet condition

$$\Psi(R_2, \theta, \phi) = 0. \tag{B2}$$

Equation B2 implies, from Equation A4, that

$$B_{lm} = -A_{lm}R_2^{2l+1}. (B3)$$

In the PFSS, B_{θ} and B_{ϕ} are not constrained by their measured values at R_1 . Thus, the general solution for the radial magnetic field component in the region $R_1 \leq r \leq R_2$ is:

$$\frac{\partial \Psi}{\partial r} = -B_r(r, \theta, \phi) = \sum_{l=0}^{\infty} \sum_{m=-l}^{l} \left[l A_{lm} r^{l-1} + (l+1) A_{lm} R_2^{2l+1} r^{-(l+2)} \right] Y_{lm}(\theta, \phi)
= \sum_{l=0}^{\infty} \sum_{m=-l}^{l} A_{lm} Y_{lm}(\theta, \phi) \left(l r^{l-1} + l R_2^{2l+1} r^{-(l+2)} + R_2^{2l+1} r^{-(l+2)} \right).$$
(B4)

To get the coefficients A_{lm} , the orthogonality condition in Equation A5 can be employed by multiplying both sides of Equation B4 by $\sin \theta Y_{l'm'}^*(\theta,\phi)$, evaluating at $r=R_1$ using boundary condition Equation B1, and integrating over θ and ϕ :

$$\int_{0}^{\pi} d\phi \int_{0}^{2\pi} d\theta \sin \theta Y_{l'm'}^{*}(\theta, \phi) B_{r}(R_{1}, \theta, \phi) = \sum_{l=0}^{\infty} \sum_{m=-l}^{l} \left(l R_{1}^{l-1} + l R_{2}^{2l+1} R_{1}^{-(l+2)} + R_{2}^{2l+1} R_{1}^{-(l+2)} \right) \times A_{lm} \int_{0}^{\pi} d\phi \int_{0}^{2\pi} d\theta \sin \theta Y_{l'm'}^{*}(\theta, \phi) Y_{lm}(\theta, \phi), \tag{B5}$$

so that

$$\int_0^{\pi} d\phi \int_0^{2\pi} d\theta \sin\theta Y_{l'm'}^*(\theta,\phi) B_r(R_1,\theta,\phi) = \sum_{l=0}^{\infty} \sum_{m=-l}^{l} \left(lR_1^{l-1} + lR_2^{2l+1} R_1^{-(l+2)} + R_2^{2l+1} R_1^{-(l+2)} \right) A_{lm} \delta_{l'l} \delta_{m'm}.$$
 (B6)

The Kroenecker δ 's force all contributions to the double sums to vanish except l = l' and m = m', whence we can write (dropping, for simplicity of notation, the primes on l and m):

$$\int_0^{\pi} d\phi \int_0^{2\pi} d\theta \sin\theta Y_{lm}^*(\theta,\phi) B_r(R_1,\theta,\phi) = A_{lm} \left(lR_1^{l-1} + lR_2^{2l+1} R_1^{-(l+2)} + R_2^{2l+1} R_1^{-(l+2)} \right).$$
 (B7)

This expression can be solved for A_{lm} by rearranging:

$$A_{lm} = \frac{a_{lm}}{lR_1^{l-1} + lR_2^{2l+1}R_1^{-(l+2)} + R_2^{2l+1}R_1^{-(l+2)}}$$
(B8)

where we have defined

$$a_{lm} \equiv \int_0^{\pi} d\phi \int_0^{2\pi} d\theta \sin\theta Y_{lm}^*(\theta, \phi) B_r(R_1, \theta, \phi). \tag{B9}$$

The radial magnetic field in the volume, Equation B4, can then be written as:

$$B_{r,pfss}(r,\theta,\phi) = \sum_{l=0}^{\infty} \sum_{m=-l}^{l} a_{lm} Y_{lm}(\theta,\phi) \frac{lr^{l-1} + lR_2^{2l+1} r^{-(l+2)} + R_2^{2l+1} r^{-(l+2)}}{lR_1^{l-1} + lR_2^{2l+1} R_1^{-(l+2)} + R_2^{2l+1} R_1^{-(l+2)}}$$

$$= \sum_{l=0}^{\infty} \sum_{m=-l}^{l} a_{lm} Y_{lm}(\theta,\phi) \left(\frac{R_1}{r}\right)^{(l+2)} \left(\frac{l(r/R_2)^{2l+1} + l + 1}{l(R_1/R_2)^{2l+1} + l + 1}\right)$$

$$\equiv \sum_{l=0}^{\infty} \sum_{m=-l}^{l} a_{lm} c_l(r) Y_{lm}(\theta,\phi).$$
(B10)

For completeness, the other two components of the magnetic field can be derived from Equation A7-Equation A8 as:

$$B_{\theta, pfss}(r, \theta, \phi) = \sum_{l=0}^{\infty} \sum_{m=-l}^{l} a_{lm} d_{l}(r) \frac{\partial Y_{lm}(\theta, \phi)}{\partial \theta},$$
(B11)

$$B_{\phi,pfss}(r,\theta,\phi) = \sum_{l=0}^{\infty} \sum_{m=-l}^{l} i \ m \ a_{lm} d_l(r) \frac{Y_{lm}(\theta,\phi)}{\sin \theta}. \tag{B12}$$

Here we have defined (cf.; Wang & Sheeley 1992; Song 2023)

$$c_l(r) \equiv \left(\frac{R_1}{r}\right)^{(l+2)} \left(\frac{l(r/R_2)^{2l+1} + l + 1}{l(R_1/R_2)^{2l+1} + l + 1}\right),\tag{B13}$$

and

$$d_l(r) \equiv -\left(\frac{R_1}{r}\right)^{l+2} \left(\frac{(r/R_2)^{2l+1} - 1}{l(R_1/R_2)^{2l+1} + l + 1}\right).$$
(B14)

At $r = R_2$, $d_l(r) = 0 \,\forall l$, making $B_{\theta}(R_2, \theta, \phi) = B_{\phi}(R_2, \theta, \phi) = 0$.

C. THE SCHATTEN CURRENT SHEET MODEL

In the Schatten (1971) model, the magnetic field $B=-\nabla\Psi$ inside the region $R_2 \leq r < \infty$, is also assumed to be potential, so Equation A3 is solved again. This time, the boundary conditions on Ψ are the Neumann boundary condition at R_2 ³:

$$\left. \frac{\partial \Psi}{\partial r}(r, \theta, \phi) \right|_{R_2} = |B_{r, pfss}(R_2, \theta, \phi)| \hat{\mathbf{r}}, \tag{C1}$$

and the Dirichlet condition

$$\Psi(r \to \infty, \theta, \phi) = 0. \tag{C2}$$

The absolute value in Equation C1 is a key feature of the Schatten model. After the general solution is calculated, locations connected by the magnetic field to locations on R_2 having $B_r(R_2, \theta, \phi) < 0$ return to their original polarity.

³ The fact that the PFSS model uses a Dirichlet condition at R_2 , while the Schatten model uses a Neumann boundary condition at R_2 creates a discontinuity in the value of Ψ . The result of the implementation of the Schatten model is the formation of a large current sheet at R_2 , so $B \neq -\nabla \Psi$ at R_2 , and the magnetic field is not irrotational there. The magnetic field is, therefore, not singular at R_2 .

The general expression for the three magnetic field components given in Equation A6-Equation A8 requires that, to satisfy Equation C2, we must have

$$A_{lm} = \delta_{l0},\tag{C3}$$

since otherwise the magnetic field will blow up as $r \to \infty$. Thus, Equation A6-Equation A8 become:

$$B_r = \sum_{l=0}^{\infty} \sum_{m=-l}^{l} \left[(l+1)B_{lm}r^{-(l+2)} \right] Y_{lm}(\theta, \phi), \tag{C4}$$

$$B_{\theta} = -\sum_{l=0}^{\infty} \sum_{m=-l}^{l} \left[B_{lm} r^{-(l+2)} \right] \frac{\partial Y_{lm}(\theta, \phi)}{\partial \theta}, \tag{C5}$$

$$B_{\phi} = -\sum_{l=0}^{\infty} \sum_{m=-l}^{l} \left[B_{lm} r^{-(l+2)} \right] im Y_{lm}(\theta, \phi).$$
 (C6)

The coefficients B_{lm} are determined by multiplying Equation C4 by $\sin \theta Y_{l'm'}^*(\theta, \phi)$, evaluating at R_2 using Equation C1, and integrating over θ and ϕ :

$$\int_{0}^{\pi} d\phi \int_{0}^{2\pi} d\theta \sin \theta Y_{l'm'}^{*}(\theta, \phi) |B_{r,pfss}(R_{2}, \theta, \phi)| = \sum_{l=0}^{\infty} \sum_{m=-l}^{l} \left[(l+1)B_{lm}R_{2}^{-(l+2)} \right] \int_{0}^{\pi} d\phi \int_{0}^{2\pi} d\theta \sin \theta Y_{l'm'}^{*}(\theta, \phi) Y_{lm}(\theta, \phi).$$
(C7)

The orthonormality of the spherical harmonics in Equation A5 yields:

$$\int_0^{\pi} d\phi \int_0^{2\pi} d\theta \sin \theta Y_{l'm'}^*(\theta, \phi) |B_{r,pfss}(R_2, \theta, \phi)| = \sum_{l=0}^{\infty} \sum_{m=-l}^{l} (l+1) B_{lm} R_2^{-(l+2)} \delta_{l'l} \delta_{m'm}.$$
 (C8)

The Kroenecker δ 's force all contributions to the double sums to vanish except l = l' and m = m', and we can once again drop the primes on l and m to write:

$$\int_{0}^{\pi} d\phi \int_{0}^{2\pi} d\theta \sin \theta Y_{lm}^{*}(\theta, \phi) |B_{r,pfss}(R_{2}, \theta, \phi)| = (l+1)B_{lm}R_{2}^{-(l+2)}.$$
 (C9)

This results in the expression for B_{lm}

$$B_{lm} = \frac{b_{lm}}{(l+1)R_2^{-(l+2)}},\tag{C10}$$

where we have defined

$$b_{lm} \equiv \int_0^{\pi} d\phi \int_0^{2\pi} d\theta \sin\theta Y_{lm}^*(\theta, \phi) |B_{r,pfss}(R_2, \theta, \phi)|.$$
 (C11)

The expression for the three magnetic field components outside R_2 then becomes:

$$B_{r,sch} = \sum_{l=0}^{\infty} \sum_{m=-l}^{l} g_l(r) b_{lm} Y_{lm}(\theta, \phi),$$
 (C12)

$$B_{\theta,sch} = -\sum_{l=0}^{\infty} \sum_{m=-l}^{l} h_l(r) \ i \ m \ b_{lm} \frac{\partial Y_{lm}(\theta,\phi)}{\partial \theta}, \tag{C13}$$

$$B_{\phi,sch} = -\sum_{l=0}^{\infty} \sum_{m=-l}^{l} h_l(r) \ i \ m \ b_{lm} Y_{lm}(\theta, \phi), \tag{C14}$$

where

$$g_l(r) \equiv \left(\frac{R_2}{r}\right)^{(l+2)},$$
 (C15)

and

$$h_l(r) \equiv \left(\frac{R_2}{r}\right)^{(l+2)} \frac{1}{l+1}.\tag{C16}$$

Note also that the transformation $R_2 \to \infty$ and $R_1 \to R_2$ makes $c_l(r) = g_l(r)$ and $d_l(r) = h_l(r)$. In this way, the Schatten model reduces to yet another implementation of the PFSS, with the outer boundary at infinity.

At this stage, all fields rooted in negative B_r at R_2 are reversed back to their original polarities. This requires tracing numerous field lines to obtain the sign of the field in the region $r > R_2$. This key step is the source of the heliospheric current sheet in the Schatten current sheet model, as the change in the direction of the magnetic field produces a large $\nabla \times \mathbf{B}$, creating a large current sheet separating positive and negative polarity regions.

An important point about the Schatten model is that while B_r is continuous across R_2 , B_θ and B_ϕ are not, since setting $r = R_2$ in Equation C13-Equation C14 of the Schatten model does not make B_θ and B_ϕ vanish. This is incompatible with the imposed boundary condition at R_2 in the PFSS, where B_θ and B_ϕ are explicitly set to 0. There is, therefore, a nonzero B_θ and B_ϕ at R_2 in the Schatten model, while the PFSS model results in $B_\theta = B_\phi = 0$ at R_2 . Mathematically, this results from using a Dirichlet condition at R_2 when solving the Laplace equation in the region $R_1 < r < R_2$, but a Neumman condition at R_2 when solving the same equation in the region $r > R_2$. Physically, this occurs because a potential field requires sources (currents) outside the domain of interest (Schuck et al. 2022), which the PFSS places inside or at the photosphere and outside the source surface. The Schatten model puts all of the sources (currents) inside the source surface and at the heliospheric current sheet. These sets of currents are fundamentally inconsistent with the idea that the only current is in the heliospheric current sheet. In fact, there is another current sheet at R_2 , so this setup cannot result in a continuous solution across the source surface for all magnetic field components.

To deal with this issue, several authors (Schatten et al. 1969; Reiss et al. 2019) perform a minimization procedure to minimize the least squared residual between the field at R_2 obtained by the SCS model (Equation C12-Equation C14) and that determined from the PFSS. This process changes the coefficients a_{lm} and b_{lm} from those determined above in a way that minimizes the error in B_r , B_θ and B_ϕ . This procedure is described in detail in Schatten et al. (1969) and Reiss et al. (2019). In this work, we do not perform such a minimization, though it may be the subject of future improvements for this model. Instead, we take the radial magnetic field at the source surface from the PFSS model (shown in Figure 11, top left) to calculate the Schatten model. Then we take the radial field at $r = 21.5R_{\odot}$ from the Schatten model as the inner boundary condition for GAMERA (shown in Figure 11, top right), with $B_{\theta} = 0$ and B_{ϕ} specified by Equation 2.11. The value of $B_{\theta,sch}$ and $B_{\phi,sch}$ from Equation C13 and Equation C14 are found to be about two orders of magnitude smaller than the value of $B_{r,sch}$ from Equation C12, so this approximation can be justified a posteriori. The velocity at the source surface (computed on a regular grid from Equation 2.6) and at the GAMERA inner boundary is also shown in the bottom panels of Figure 11 for context. The velocity on the inner boundary is plotted by tracing field lines from a regular grid on the inner boundary down to the source surface, where the velocity has been computed from Equation 2.6, and taking the values of the velocity at the locations of the field line footpoints on the source surface.

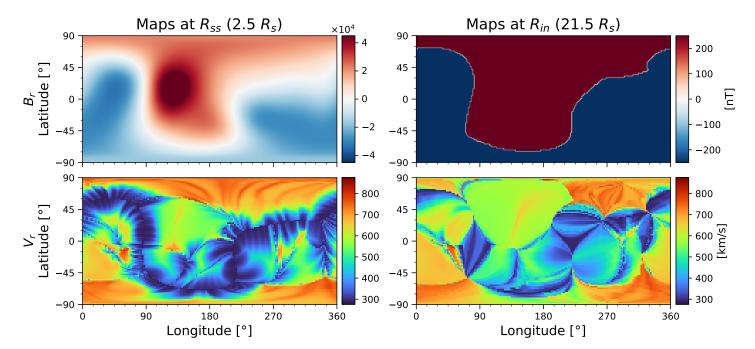


Figure 11. Radial magnetic field (top) and radial velocity (bottom) calculated from the PFSS and WSA velocity equation models using ADAPT data, respectively, at the source surface (left) and as extrapolated to the GAMERA inner boundary (right). The right panels are the same as in Figure 2, though without the open flux contours in the B_r panel, and are shown for comparison.

Software: Astropy (The Astropy Collaboration et al. 2018), h5py (Collette 2013), IPython (Pérez & Granger 2007), Matplotlib (Hunter 2007), Numpy (Oliphant 2006), Pandas (pandas development team 2020), Scipy (Virtanen et al. 2020), SpiceyPy (Annex et al. 2020).

REFERENCES

- Abbo, L., Ofman, L., Antiochos, S. K., et al. 2016, Space Sci. Rev., 201, 55, doi: 10.1007/s11214-016-0264-1
- Altschuler, M. D., & Newkirk, G. 1969, Solar Physics, 9, 131
- Annex, A., Pearson, B., Seignovert, B., et al. 2020, The Journal of Open Source Software, 5, 2050, doi: 10.21105/joss.02050
- Antiochos, S. K., Mikić, Z., Titov, V. S., Lionello, R., & Linker, J. A. 2011, ApJ, 731, 112, doi: 10.1088/0004-637X/731/2/112
- Arge, C. N., Henney, C. J., Hernandez, I. G., et al. 2013, in American Institute of Physics Conference Series, Vol. 1539, Solar Wind 13, ed. G. P. Zank, J. Borovsky,
 - R. Bruno, J. Cirtain, S. Cranmer, H. Elliott,
 - J. Giacalone, W. Gonzalez, G. Li, E. Marsch,
 - E. Moebius, N. Pogorelov, J. Spann, &
 - O. Verkhoglyadova, 11-14, doi: 10.1063/1.4810977
- Arge, C. N., Henney, C. J., Koller, J., et al. 2010, in
 American Institute of Physics Conference Series, Vol. 1216, Twelfth International Solar Wind Conference, ed. M. Maksimovic, K. Issautier, N. Meyer-Vernet,
 M. Moncuquet, & F. Pantellini, 343–346,
 doi: 10.1063/1.3395870
- Arge, C. N., Leisner, A., Wallace, S., & Henney, C. J. 2023, arXiv e-prints, arXiv:2304.07649, doi: 10.48550/arXiv.2304.07649
- Arge, C. N., & Pizzo, V. J. 2000, J. Geophys. Res., 105, 10465, doi: 10.1029/1999JA000262
- Asplund, M., Grevesse, N., Sauval, A. J., & Scott, P. 2009, ARA&A, 47, 481,
 - doi: 10.1146/annurev.astro.46.060407.145222
- Badman, S. T., Bale, S. D., Martínez Oliveros, J. C., et al. 2020, ApJS, 246, 23, doi: 10.3847/1538-4365/ab4da7
- Badman, S. T., Bale, S. D., Rouillard, A. P., et al. 2021, A&A, 650, A18, doi: 10.1051/0004-6361/202039407
- Badman, S. T., Brooks, D. H., Poirier, N., et al. 2022, ApJ, 932, 135, doi: 10.3847/1538-4357/ac6610
- Badman, S. T., Riley, P., Jones, S. I., et al. 2023, Journal of Geophysical Research (Space Physics), 128, e2023JA031359, doi: 10.1029/2023JA031359
- Bale, S. D., Goetz, K., Harvey, P. R., et al. 2016,Space Sci. Rev., 204, 49, doi: 10.1007/s11214-016-0244-5
- Barnes, G., DeRosa, M. L., Jones, S. I., et al. 2023, arXiv e-prints, arXiv:2302.06496.
 - https://arxiv.org/abs/2302.06496
- Brooks, D. H., Ugarte-Urra, I., & Warren, H. P. 2015, Nature Communications, 6, 5947, doi: 10.1038/ncomms6947

- Brooks, D. H., & Warren, H. P. 2011, ApJ, 727, L13, doi: 10.1088/2041-8205/727/1/L13
- Caplan, R. M., Downs, C., & Linker, J. A. 2016, ApJ, 823, 53, doi: 10.3847/0004-637X/823/1/53
- Case, A. W., Kasper, J. C., Stevens, M. L., et al. 2020, ApJS, 246, 43, doi: 10.3847/1538-4365/ab5a7b
- Chhiber, R., Usmanov, A. V., Matthaeus, W. H., & Goldstein, M. L. 2021, ApJ, 923, 89, doi: 10.3847/1538-4357/ac1ac7
- Collette, A. 2013, Python and HDF5 (O'Reilly)
- Culhane, J. L., Harra, L. K., James, A. M., et al. 2007, Sol. Phys., 243, 19, doi: 10.1007/s01007-007-0293-1
- Culhane, J. L., Brooks, D. H., van Driel-Gesztelyi, L., et al. 2014, Sol. Phys., 289, 3799,
 - doi: 10.1007/s11207-014-0551-5
- Dakeyo, J.-B., Maksimovic, M., Démoulin, P., Halekas, J., & Stevens, M. L. 2022, ApJ, 940, 130, doi: 10.3847/1538-4357/ac9b14
- De Pontieu, B., Title, A. M., Lemen, J. R., et al. 2014, Sol. Phys., 289, 2733, doi: 10.1007/s11207-014-0485-y
- Del Zanna, G. 2008, A&A, 481, L49, doi: 10.1051/0004-6361:20079087
- Domingo, V., Fleck, B., & Poland, A. I. 1995,Space Sci. Rev., 72, 81, doi: 10.1007/BF00768758
- Doschek, G. A., Warren, H. P., Mariska, J. T., et al. 2008, ApJ, 686, 1362, doi: 10.1086/591724
- Drake, J. F., Agapitov, O., Swisdak, M., et al. 2021, A&A, 650, A2, doi: 10.1051/0004-6361/202039432
- Driesman, A., Hynes, S., & Cancro, G. 2008,
 Space Sci. Rev., 136, 17, doi: 10.1007/s11214-007-9286-z
 Feldman, U. 1992, Phys. Scr, 46, 202,
 doi: 10.1088/0031-8949/46/3/002
- Fox, N. J., Velli, M. C., Bale, S. D., et al. 2016,Space Sci. Rev., 204, 7, doi: 10.1007/s11214-015-0211-6
- Fränz, M., & Harper, D. 2002, Planet. Space Sci., 50, 217, doi: 10.1016/S0032-0633(01)00119-2
- Gosling, J. T. 1997, in American Institute of Physics Conference Series, Vol. 385, Robotic Exploration Close to the Sun: Scientific Basis, ed. S. R. Habbal, 17–24, doi: 10.1063/1.51743
- Grevesse, N., & Sauval, A. J. 1998, Space Sci. Rev., 85, 161, doi: 10.1023/A:1005161325181
- Harra, L., Brooks, D. H., Bale, S. D., et al. 2021, A&A, 650, A7, doi: 10.1051/0004-6361/202039514
- Harvey, J., Gillespie, B., Miedaner, P., & Slaughter, C. 1980, Synoptic solar magnetic field maps for the interval including Carrington Rotation 1601-1680, May 5, 1973 -April 26, 1979

- Harvey, J. W., Hill, F., Hubbard, R. P., et al. 1996,Science, 272, 1284, doi: 10.1126/science.272.5266.1284
- Hathaway, D. H., Upton, L. A., & Mahajan, S. S. 2022, Frontiers in Astronomy and Space Sciences, 9, 1007290, doi: 10.3389/fspas.2022.1007290
- Hathaway, D. H., Williams, P. E., Dela Rosa, K., & Cuntz, M. 2010, ApJ, 725, 1082, doi: 10.1088/0004-637X/725/1/1082
- Hickmann, K. S., Godinez, H. C., Henney, C. J., & Arge,C. N. 2015, Sol. Phys., 290, 1105,doi: 10.1007/s11207-015-0666-3
- Higginson, A. K., Antiochos, S. K., DeVore, C. R., Wyper,
 P. F., & Zurbuchen, T. H. 2017, ApJ, 840, L10,
 doi: 10.3847/2041-8213/aa6d72
- Horbury, T. S., O'Brien, H., Carrasco Blazquez, I., et al. 2020, A&A, 642, A9, doi: 10.1051/0004-6361/201937257
- Howard, R. A., Moses, J. D., Vourlidas, A., et al. 2008, Space Sci. Rev., 136, 67, doi: 10.1007/s11214-008-9341-4
- Hundhausen, A. J. 1977, in Coronal Holes and High Speed Wind Streams, ed. J. B. Zirker, 225–329
- Hunter, J. D. 2007, Computing in Science & Engineering, 9, 90, doi: 10.1109/MCSE.2007.55
- Jackson, B. V. 1985, Sol. Phys., 95, 363, doi: 10.1007/BF00152413
- Jackson, J. D. 1998, Classical Electrodynamics (Wiley)
- Jivani, A., Sachdeva, N., Huang, Z., et al. 2023, Space Weather, 21, e2022SW003262,
 - doi: https://doi.org/10.1029/2022SW003262
- Kasper, J. C., Abiad, R., Austin, G., et al. 2016, Space Sci. Rev., 204, 131, doi: 10.1007/s11214-015-0206-3
- Kim, T. K., Pogorelov, N. V., Arge, C. N., et al. 2020, ApJS, 246, 40, doi: 10.3847/1538-4365/ab58c9
- Kosugi, T., Matsuzaki, K., Sakao, T., et al. 2007,Sol. Phys., 243, 3, doi: 10.1007/s11207-007-9014-6
- Lemen, J. R., Title, A. M., Akin, D. J., et al. 2012, Solar Physics, 275, 17, doi: 10.1007/s11207-011-9776-8
- Lepping, R. P., Acūna, M. H., Burlaga, L. F., et al. 1995, Space Sci. Rev., 71, 207, doi: 10.1007/BF00751330
- Linker, J. A., Caplan, R. M., Downs, C., et al. 2017, ApJ, 848, 70, doi: 10.3847/1538-4357/aa8a70
- Lionello, R., Velli, M., Downs, C., Linker, J. A., & Mikić, Z. 2014, ApJ, 796, 111, doi: 10.1088/0004-637X/796/2/111
- Livi, R., Larson, D. E., Kasper, J. C., et al. 2022, ApJ, 938, 138, doi: 10.3847/1538-4357/ac93f5
- Livi, S., Lepri, S. T., Raines, J. M., et al. 2023, A&A, 676, A36, doi: 10.1051/0004-6361/202346304
- Louarn, P., fedorov, a., & Owen, C. 2020, in EGU General Assembly Conference Abstracts, EGU General Assembly Conference Abstracts, 4720,
 - doi: 10.5194/egusphere-egu2020-4720

- Lyon, J. G., Fedder, J. A., & Mobarry, C. M. 2004, Journal of Atmospheric and Solar-Terrestrial Physics, 66, 1333, doi: 10.1016/j.jastp.2004.03.020
- MacNeice, P., Elliott, B., & Acebal, A. 2011, Space Weather, 9, S10003, doi: 10.1029/2011SW000665
- McComas, D. J., Alexander, N., Angold, N., et al. 2016, Space Sci. Rev., 204, 187, doi: 10.1007/s11214-014-0059-1
- McGregor, S. L. 2011, On tracing the origins of the solar wind (Boston University)
- Merkin, V., Lionello, R., Lyon, J., et al. 2016, The Astrophysical Journal, 831, 23
- Merkin, V. G., Lyon, J. G., Lario, D., Arge, C. N., & Henney, C. J. 2016, Journal of Geophysical Research (Space Physics), 121, 2866, doi: 10.1002/2015JA022200
- Merkin, V. G., Lyon, J. G., McGregor, S. L., & Pahud, D. M. 2011, Geophysical Research Letters, 38, n/a, doi: 10.1029/2011gl047822
- Möestl, C., Weiss, A. J., Bailey, R. L., & Reiss, M. A. 2023, HELIO4CAST Interplanetary Coronal Mass Ejection Catalog v2.1, doi: 10.6084/m9.figshare.6356420.v15
- Mostafavi, P., Merkin, V. G., Provornikova, E., et al. 2022, ApJ, 925, 181, doi: 10.3847/1538-4357/ac3fb4
- Müller, D., Marsden, R. G., St. Cyr, O. C., Gilbert, H. R., & Solar Orbiter Team. 2013, Sol. Phys., 285, 25, doi: 10.1007/s11207-012-0085-7
- Müller, D., St. Cyr, O. C., Zouganelis, I., et al. 2020, A&A, 642, A1, doi: 10.1051/0004-6361/202038467
- Nolte, J. T., & Roelof, E. C. 1973, Sol. Phys., 33, 241, doi: 10.1007/BF00152395
- Odstrcil, D. 2003, Advances in Space Research, 32, 497, doi: 10.1016/S0273-1177(03)00332-6
- Ogilvie, K. W., Durney, A., & von Rosenvinge, T. T. 1978, IEEE Transactions on Geoscience Electronics, 3, 151
- Ogilvie, K. W., Chornay, D. J., Fritzenreiter, R. J., et al. 1995, Space Sci. Rev., 71, 55, doi: 10.1007/BF00751326
- Oliphant, T. 2006, A Guide to Numpy (USA: Trelgol Publishing)
- Owen, C. J., Bruno, R., Livi, S., et al. 2020, A&A, 642, A16, doi: 10.1051/0004-6361/201937259
- Owocki, S. P., Holzer, T. E., & Hundhausen, A. J. 1983, ApJ, 275, 354, doi: 10.1086/161538
- pandas development team, T. 2020, pandas-dev/pandas: Pandas, latest, Zenodo, doi: 10.5281/zenodo.3509134
- Papitashvili, N. E., & King, J. H. 2020, OMNI Hourly Data", NASA Space Physics Data Facility, doi: 10.48322/1shr-ht18

- Paularena, K. I., & King, J. H. 1999, in NATO Advanced
 Study Institute (ASI) Series C, Vol. 537, Interball in the
 ISTP Program: Studies of the Solar
 Wind-Magnetosphere-Ionosphere Interaction, ed. D. G.
 Sibeck & K. Kudela, 145
- Pecora, F., Matthaeus, W. H., Primavera, L., et al. 2022, ApJ, 929, L10, doi: 10.3847/2041-8213/ac62d4
- Pérez, F., & Granger, B. E. 2007, Computing in Science & Engineering, 9, 21, doi: 10.1109/MCSE.2007.53
- Perri, B., Leitner, P., Brchnelova, M., et al. 2022, ApJ, 936, 19, doi: 10.3847/1538-4357/ac7237
- Pinto, R. F., & Rouillard, A. P. 2017, ApJ, 838, 89, doi: 10.3847/1538-4357/aa6398
- Pogorelov, N. V. 2020, Proceedings of the International Astronomical Union, 16, 309–323, doi: 10.1017/S1743921322001612
- Pomoell, J., & Poedts, S. 2018, Journal of Space Weather and Space Climate, 8, A35, doi: 10.1051/swsc/2018020
- Raouafi, N. E., Matteini, L., Squire, J., et al. 2023, Space Sci. Rev., 219, 8, doi: 10.1007/s11214-023-00952-4
- Reiss, M. A., MacNeice, P. J., Mays, L. M., et al. 2019, ApJS, 240, 35, doi: 10.3847/1538-4365/aaf8b3
- Riley, P., Linker, J. A., Lionello, R., & Mikic, Z. 2012, Journal of Atmospheric and Solar-Terrestrial Physics, 83, 1, doi: 10.1016/j.jastp.2011.12.013
- Riley, P., Linker, J. A., & Mikić, Z. 2013, Journal of Geophysical Research (Space Physics), 118, 600, doi: 10.1002/jgra.50156
- Riley, P., Lionello, R., Caplan, R. M., et al. 2021, A&A, 650, A19, doi: 10.1051/0004-6361/202039815
- Rochus, P., Auchère, F., Berghmans, D., et al. 2020, A&A, 642, A8, doi: 10.1051/0004-6361/201936663
- Roša, D., Brajša, R., Vršnak, B., & Wöhl, H. 1995,Sol. Phys., 159, 393, doi: 10.1007/BF00686540
- Sakao, T., Kano, R., Narukage, N., et al. 2007, Science, 318, 1585, doi: 10.1126/science.1147292
- Samara, Pinto, R. F., Magdaleni´c, J., et al. 2021, A&A, 648, A35, doi: 10.1051/0004-6361/202039325
- Samara, E., Arge, C. N., Pinto, R. F., et al. 2022, in EGU General Assembly Conference Abstracts, EGU General Assembly Conference Abstracts, EGU22–9583, doi: 10.5194/egusphere-egu22-9583
- Sanchez-Diaz, E., Rouillard, A. P., Lavraud, B., et al. 2016, Journal of Geophysical Research: Space Physics, 121, 2830, doi: https://doi.org/10.1002/2016JA022433
- Schatten, K. H. 1971, Cosmic Electrodynamics, 2, 232 Schatten, K. H., Wilcox, J. M., & Ness, N. F. 1969, Solar
- Schatten, K. H., Wilcox, J. M., & Ness, N. F. 1969, Solar Physics, 6, 442
- Scherrer, P. H., Schou, J., Bush, R. I., et al. 2012, Solar Physics, 275, 207, doi: 10.1007/s11207-011-9834-2

- Schrijver, C. J., & Title, A. M. 2001, ApJ, 551, 1099, doi: 10.1086/320237
- Schuck, P. W., Linton, M. G., Knizhnik, K. J., & Leake, J. E. 2022, ApJ, 936, 94, doi: 10.3847/1538-4357/ac739a
- Simon, G. W., Title, A. M., & Weiss, N. O. 1995, ApJ, 442, 886, doi: 10.1086/175491
- Song, Y. 2023, arXiv e-prints, arXiv:2305.12124, doi: 10.48550/arXiv.2305.12124
- Sorathia, K. A., Merkin, V. G., Panov, E. V., et al. 2020, Geophys. Res. Lett., 47, e88227, doi: 10.1029/2020GL088227
- SPICE Consortium, Anderson, M., Appourchaux, T., et al. 2020, A&A, 642, A14, doi: 10.1051/0004-6361/201935574
- Stone, E. C., Frandsen, A. M., Mewaldt, R. A., et al. 1998, Space Sci. Rev., 86, 1, doi: 10.1023/A:1005082526237
- Szabo, A. 2015, in Handbook of Cosmic Hazards and Planetary Defense, 141–157, doi: 10.1007/978-3-319-03952-7_13
- Telloni, D., Romoli, M., Velli, M., et al. 2023, ApJ, 955, L4, doi: 10.3847/2041-8213/ace112
- Tenerani, A., Velli, M., Matteini, L., et al. 2020, The Astrophysical Journal Supplement Series, 246, 32, doi: 10.3847/1538-4365/ab53e1
- The Astropy Collaboration, Price-Whelan, A. M., Sipőcz, B. M., et al. 2018, The Astronomical Journal, 156, 123, doi: 10.3847/1538-3881/aabc4f
- Thompson, W. T. 2006, A&A, 449, 791, doi: 10.1051/0004-6361:20054262
- Ugarte-Urra, I., Upton, L., Warren, H. P., & Hathaway,
 D. H. 2015, ApJ, 815, 90,
 doi: 10.1088/0004-637X/815/2/90
- Ulrich, R. K., & Boyden, J. E. 2006, Sol. Phys., 235, 17, doi: 10.1007/s11207-006-0041-5
- Upton, L., & Hathaway, D. H. 2014, ApJ, 780, 5, doi: 10.1088/0004-637X/780/1/5
- Upton, L., Ugarte-Urra, I., & Warren, H. 2019, in American Astronomical Society Meeting Abstracts, Vol. 234, American Astronomical Society Meeting Abstracts #234, 118.02
- Upton, L. A., & Hathaway, D. H. 2018,Geophys. Res. Lett., 45, 8091,doi: 10.1029/2018GL078387
- van der Holst, B., Sokolov, I. V., Meng, X., et al. 2014, ApJ, 782, 81, doi: 10.1088/0004-637X/782/2/81
- van der Holst, B., Huang, J., Sachdeva, N., et al. 2022, ApJ, 925, 146, doi: 10.3847/1538-4357/ac3d34
- Virtanen, I., & Mursula, K. 2017, A&A, 604, A7, doi: 10.1051/0004-6361/201730863
- Virtanen, P., Gommers, R., Oliphant, T. E., et al. 2020, Nature Methods, 1, doi: 10.1038/s41592-019-0686-2

Vourlidas, A., Howard, R. A., Plunkett, S. P., et al. 2016, Space Sci. Rev., 204, 83, doi: 10.1007/s11214-014-0114-y

- Wallace, S., Arge, C. N., Viall, N., & Pihlström, Y. 2020, ApJ, 898, 78, doi: 10.3847/1538-4357/ab98a0
- --. 2021, ApJ, 919, 68, doi: 10.3847/1538-4357/ac2512
- Wallace, S., Jones, S. I., Arge, C. N., Viall, N. M., & Henney, C. J. 2022, ApJ, 935, 24, doi: 10.3847/1538-4357/ac731c
- Wang, Y. M., & Sheeley, N. R., J. 1990, ApJ, 355, 726, doi: 10.1086/168805
- —. 1992, ApJ, 392, 310, doi: 10.1086/171430
- —. 1994, ApJ, 430, 399, doi: 10.1086/174415
- Wenzel, K. P., Marsden, R. G., Page, D. E., & Smith, E. J. 1992, A&AS, 92, 207
- Worden, J., & Harvey, J. 2000, Sol. Phys., 195, 247, doi: 10.1023/A:1005272502885
- Wu, C.-C., & Dryer, M. 1997, Sol. Phys., 173, 391, doi: 10.1023/A:1004929802499
- Wu, C.-C., Dryer, M., Wu, S. T., et al. 2011, Journal of Geophysical Research (Space Physics), 116, A12103, doi: 10.1029/2011JA016947

- Wu, C.-C., Fry, C. D., Wu, S. T., Dryer, M., & Liou, K. 2007, Journal of Geophysical Research (Space Physics), 112, A09104, doi: 10.1029/2006JA012211
- Wu, C.-C., Liou, K., Lepping, R. P., et al. 2016a, Earth, Planets and Space, 68, 151, doi: 10.1186/s40623-016-0525-y
- Wu, C.-C., Liou, K., Vourlidas, A., et al. 2016b, Journal of Geophysical Research (Space Physics), 121, 56, doi: 10.1002/2015JA021051
- Wu, C.-C., Liou, K., & Warren, H. 2020, Sol. Phys., 295, 25, doi: 10.1007/s11207-019-1576-6
- Zhang, B., Sorathia, K. A., Lyon, J. G., et al. 2019, ApJS, 244, 20, doi: 10.3847/1538-4365/ab3a4c
- Zhao, L., Zurbuchen, T. H., & Fisk, L. A. 2009, Geophys. Res. Lett., 36, L14104, doi: 10.1029/2009GL039181
- Zirker, J. B. 1977, Reviews of Geophysics and Space Physics, 15, 257, doi: 10.1029/RG015i003p00257